JACS Au
AN OPEN ACCESS JOURNAL OF THE AMERICAN CHEMICAL SOCIETY

pubs.acs.org/jacsau

Article

Endogenous Conjugation of Biomimetic Dinitrosyl Iron Complex with Protein Vehicles for Oral Delivery of Nitric Oxide to Brain and Activation of Hippocampal Neurogenesis

Cheng-Ru Wu,[○] Yi-Da Huang,[○] Yong-Huei Hong, Ya-Hsin Liu, Manmath Narwane, Yu-Hsiang Chang, Trinh Kieu Dinh, Hsin-Tzu Hsieh, Yi-Jen Hseuh, Ping-Ching Wu, Chih-Wen Pao, Ting-Shan Chan, I-Jui Hsu, Yunching Chen, Hung-Chi Chen,* Ting-Yu Chin,* and Tsai-Te Lu*

Cite This: *JACS Au* 2021, 1, 998–1013

Read Online

ACCESS | Metrics & More | Article Recommendations | Supporting Information

ABSTRACT: Nitric oxide (NO), a pro-neurogenic and antineuroinflammatory gasotransmitter, features the potential to develop a translational medicine against neuropathological conditions. Despite the extensive efforts made on the controlled delivery of therapeutic NO, however, an orally active NO prodrug for a treatment of chronic neuropathy was not reported yet. Inspired by the natural dinitrosyl iron unit (DNIU) $[Fe(NO)_2]$, in this study, a reversible and dynamic interaction between the biomimetic $[(NO)_2Fe(\mu\text{-}SCH_2CH_2OH)_2Fe(NO)_2]$ (**DNIC-1**) and serum albumin (or gastrointestinal mucin) was explored to discover endogenous proteins as a vehicle for an oral delivery of NO to the brain after an oral administration of **DNIC-1**. On the basis of the in vitro and in vivo study, a rapid binding of **DNIC-1** toward gastrointestinal mucin yielding the mucin-bound dinitrosyl iron complex (DNIC) discovers the mucoadhesive nature of **DNIC-1**. A reversible interconversion between mucin-bound DNIC and **DNIC-1** facilitates the mucus-penetrating migration of **DNIC-1** shielded in the gastrointestinal tract of the stomach and small intestine. Moreover, the NO-release reactivity of **DNIC-1** induces the transient opening of the cellular tight junction and enhances its paracellular permeability across the intestinal epithelial barrier. During circulation in the bloodstream, a stoichiometric binding of **DNIC-1** to the serum albumin, as another endogenous protein vehicle, stabilizes the DNIU $[Fe(NO)_2]$ for a subsequent transfer into the brain. With aging mice under a Western diet as a disease model for metabolic syndrome and cognitive impairment, an oral administration of **DNIC-1** in a daily manner for 16 weeks activates the hippocampal neurogenesis and ameliorates the impaired cognitive ability. Taken together, these findings disclose the synergy between biomimetic **DNIC-1** and endogenous protein vehicles for an oral delivery of therapeutic NO to the brain against chronic neuropathy.

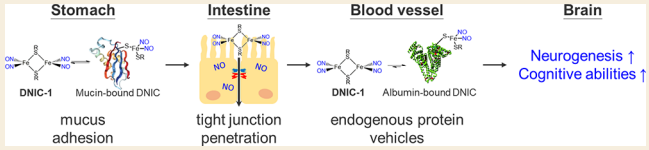

KEYWORDS: *nitric oxide, dinitrosyl iron complex, protein vehicle, drug delivery, neurogenesis*

INTRODUCTION

Nitric oxide (NO) is a small and diffusible gasotransmitter modulating neurogenesis and (anti)neuroinflammation processes in the central and peripheral nervous systems.[1,2] At an appropriate level, in particular, NO has been proved to serve as an anti-inflammatory, antiapoptotic, and pro-neurogenic reagent via the activation of the NO-soluble guanylyl cyclase (sGC)-cyclic guanosine monophosphate (cGMP) pathway.[3−5] On the one hand, to develop NO as a translational medicine for the treatment of neuropathological conditions, therefore, the spatial and dosage control of pleiotropic nitric oxide was attempted through a regulation of endogenous enzymes (i.e., neuronal nitric oxide synthase), in situ electrochemical generation of nitric oxide, and utilization of on-demand nitric oxide release molecules/materials (NORMs).[6−10] For example, daily treatment of *N*-[bis(2-aminoethyl)amino]-*N*-hydroxynitrous amide (DETA/NONOate), an exogenous NO donor, via an intraperitoneal injection upregulated neurogenesis and reduced functional deficits after a traumatic brain injury in rats.[10] On the other hand, a near-infrared light-triggered release of nitric oxide from an upconversion nanoparticle core coated by zeolitic imidazolate framework-8 (ZIF-8) with NO donor (*S*-nitrosocysteine, CysNO) suppressed inflammation and promoted neuroregeneration for the repair of a spinal cord injury.[8] To the best of our knowledge, however, an orally active NO prodrug against chronic neuropathy was not reported yet, despite an oral administration being the most prevalent, noninvasive, and convenient route for repeated dosing and good patient compliance.[11]

Critical parameters that enhance oral bioavailability of the low-molecular-weight pharmaceutics are hydrophilicity (LogP =

Received: April 9, 2021
Published: June 7, 2021

https://doi.org/10.1021/jacsau.1c00160
JACS Au 2021, 1, 998–1013

Scheme 1. Schematic Illustration of Endogenous Conjugation of Dinitrosyl Iron Complex $[(NO)_2Fe(\mu\text{-}SCH_2CH_2OH)_2Fe(NO)_2]$ (DNIC-1) with Protein Vehicles for Oral Delivery of Nitric Oxide to Brain, for Activation of Hippocampal Neurogenesis, and for Recovery of Cognitive Impairment in Aging Mice with Metabolic Syndrome

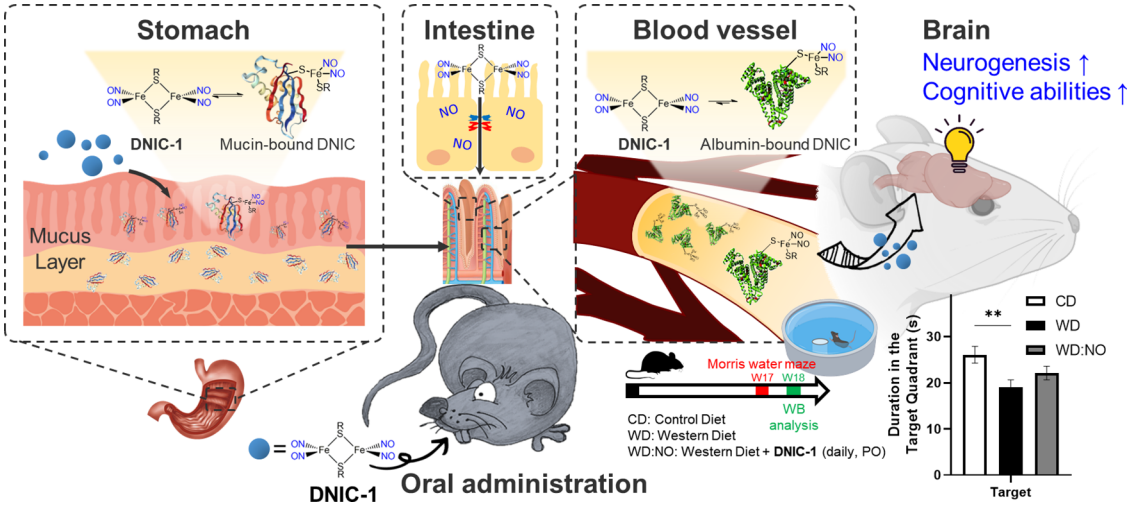

1−3) and stability under a gastric pH environment.[12,13] Moreover, a mucus layer, primarily consisting of water (~95%) and cysteine-rich mucin (~2−5% w/v), has evolved to protect the underlying epithelia from gastric acid/digestive enzymes (i.e., pepsin) and, meanwhile, builds up a barrier for the delivery of an oral drug.[14−17] Consequently, mucoadhesive and mucus-penetrating vehicles were designed to enhance the intestinal retention and to overcome the gastrointestinal (GI) mucus layer through the formation of a reversible and dynamic charge interaction or disulfide bond linkage with mucus.[16−21] In particular, the surface coating of a positively charged insulin:chitosan nanoparticle core with thiolated hyaluronic acid (HA-SH) has been reported to strengthen the mucoadhesive nature and the intestinal retention of the assembled conjugates, whereas a subsequent dissociation of the HA-SH coating from the nanoparticle when across the mucosal layer facilitates the mucus-penetration ability.[18,19]

Besides the reversible and dynamic interaction with gastrointestinal mucin boosting the oral bioavailability, endogenous and exogenous conjugations of (metallo-)pharmaceutics/metal nanoparticles with serum albumin in a (non)covalent manner were exploited to enhance the biocompatibility, to improve the pharmacokinetic profile, to penetrate the blood-brain barrier, and even to target the inflammatory and malignant sites.[22−28] Human serum albumin (HSA) is a non(immuno)toxic, stable (half-life = 19 d), and abundant plasma protein (34−55 mg/mL), which is involved in the maintenance of blood colloidal osmotic pressure and the transport of essential biomolecules such as amino acids, hormones, and fatty acids.[23,24] Through mimicking the overall features of a fatty acid, an asymmetrical functionalization of the axial ligand of the *cis,cis,trans*-$[Pt^{IV}(NH_3)_2Cl_2(O_2CCH_2CH_2COOH)(OCONHR)]$ (R = linear alkyl group) prodrugs enhanced its noncovalent binding to HSA.[29,30] A systematic variation of the length of the aliphatic tail, moreover, modulates the cellular uptake and redox profile of Pt(IV) prodrugs, of which the subsequent intracellular reduction resulted in the release of cisplatin and cytotoxicity.[29] Maleimide-functionalized Pt(IV) prodrugs were also designed to enable the covalent conjugation with endogenous HSA through a selective reaction with the single free thiol group on an accessible cysteine-34.[31,32] After an intravenous injection of Pt-based chemotherapeutics (i.e., cisplatin) to a patient, recently, the direct binding of cisplatin to HSA and the subsequent reduction by biological reductants were reported to initiate the blood-triggered generation of a Pt nanoparticle encapsulated in the HSA corona, which features a selective and long-term accumulation in the tumor site.[24,25,33]

Derived from the nitrosylation of [Fe−S] proteins or cellular chelatable iron, dinitrosyl iron unit (DNIU) $[Fe(NO)_2]$ anchored in a protein-bound form or a low-molecular-weight complex is a natural cofactor for the storage and transport of nitric oxide.[34−36] Inspired by natural DNIU $[Fe(NO)_2]$, biomimetic study was reported to explore mononuclear $\{Fe(NO)_2\}^9$ dinitrosyl iron complexes (DNICs) $[(NO)_2Fe(SR)_2]^-$ (or $[(NO)_2Fe(L)_2]^-$) featuring a distinctive electron paramagnetic resonance (EPR) signal at g = 2.03, which is consistent with protein-bound DNICs (Table S1).[37] Moreover, interconversions among mononuclear DNICs $[(NO)_2Fe(SR)_2]^-/[(NO)_2Fe(SR')_2]^-$ and dinuclear DNIC $[(NO)_2Fe(\mu\text{-}SR)_2Fe(NO)_2]$ disclosed alternative mechanisms projecting on the biological delivery of DNIU $[Fe(NO)_2]$.[36,37] On the one hand, the transfer of DNIU $[Fe(NO)_2]$ from glutathione-bound DNIC to human glutathione transferase (GST P1−1) yielding crystallographically characterized $[(NO)_2Fe(SR)(GST\text{-}Tyr7)]$ (SR = glutathione) unraveled the conversion of low-molecular-weight DNIC into the protein-bound form through a ligand exchange pathway.[38] On the other hand, the cysteine-mediated core extrusion of DNIU $[Fe(NO)_2]$ from protein-bound DNIC demonstrated the reversed transformation of protein-bound DNIC into the low-molecular-weight form.[39] Recently, the in vitro and in vivo NO-delivery reactivity of synthetic DNICs was investigated for the activation of a NO-sGC-cGMP pathway and for the treatment of inflammation, cancer, hypertension, and diabetic wound healing.[40−44] In this study, the reversible and dynamic interaction between $[(NO)_2Fe(\mu\text{-}SCH_2CH_2OH)_2Fe(NO)_2]$ (**DNIC-1**) and serum albumin (or gastrointestinal mucin) was explored to discover endogenous proteins as a vehicle for the stabilization and delivery of DNIU $[Fe(NO)_2]$ (Scheme 1). On the basis of the in vivo study, the endogenous conjugation of **DNIC-1** with mucin in the gastrointestinal mucus and albumin in the bloodstream, respectively, enables the oral delivery of nitric oxide to the brain after an oral

https://doi.org/10.1021/jacsau.1c00160
JACS Au 2021, 1, 998−1013

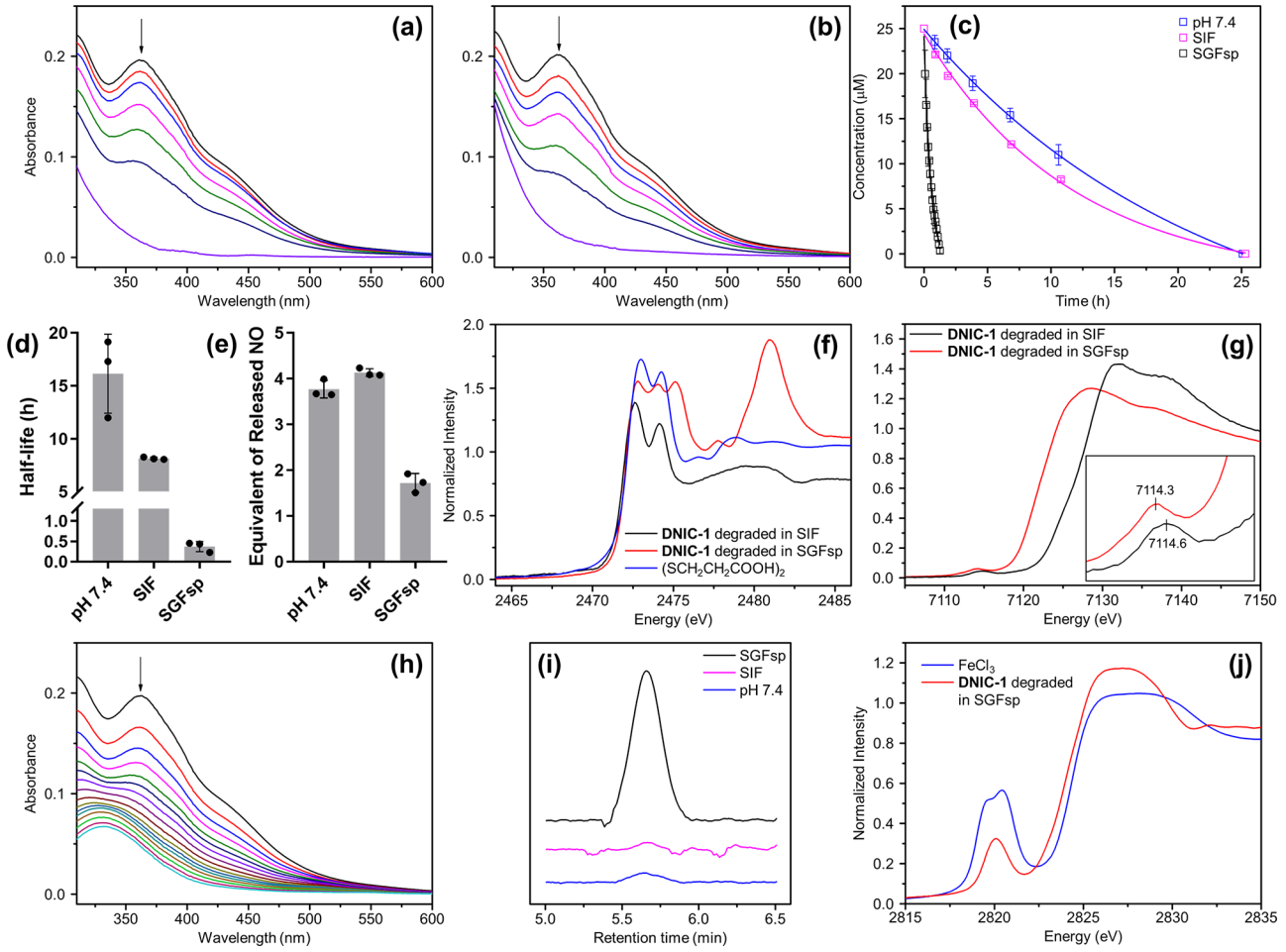

Figure 1. Mechanistic study of the pH-dependent degradation and NO-release reactivity of **DNIC-1**. Time-dependent change of UV−vis spectra for **DNIC-1** (a) at pH = 7.4 and (b) in SIF (pH 6.8). (c) Decompositions of **DNIC-1** at pH = 7.4 (blue), in SIF (magenta), and in SGFsp (black), which were fitted to pseudo-first-order kinetics. Data show the mean ± SD from three independent experiments. (d) Half-life for the pH-dependent decomposition of **DNIC-1** at 37 °C. Data represent the mean ± SD (n = 3). (e) Equivalent of released nitric oxide during the degradation of **DNIC-1**. The data are the mean values ± SD pooled from three independent experiments. (f) S and (g) Fe K-edge XAS for the degradation byproducts obtained from the decomposition of **DNIC-1** in SIF (black) and in SGFsp (red). S K-edge XAS of $(SCH_2CH_2COOH)_2$ is shown in blue. (h) Time-dependent change of UV−vis spectra for **DNIC-1** in SGFsp (pH 1.2). (i) GC chromatograms for the gaseous byproduct, $N_2O_{(g)}$, derived from the decomposition of **DNIC-1** in SGFsp (black), in SIF (magenta), and at pH = 7.4 (blue). (j) Cl K-edge XAS for the degradation byproducts obtained from the decomposition of **DNIC-1** in SIF (black) and in SGFsp (red). Cl K-edge XAS of $FeCl_3$ is shown in blue.

administration of **DNIC-1**. With a reliance on the pro-neurogenic and antineuroinflammation effect of the NO-release **DNIC-1**, moreover, the oral administration of **DNIC-1** to aging mice with a metabolic syndrome in a daily manner for 16 weeks activates hippocampal neurogenesis and improves the cognitive impairment.

RESULTS AND DISCUSSION

pH-Dependent Degradation and NO-Release Reactivity of DNIC-1

To mimic the trafficking of complex $[(NO)_2Fe(\mu\text{-}SCH_2CH_2OH)_2Fe(NO)_2]$ (**DNIC-1**) in the GI tract and blood circulation system, the stability and NO-release reactivity of **DNIC-1** in simulated gastric fluid without pepsin (SGFsp, pH 1.2), simulated intestinal fluid (SIF, pH 6.8), and 50 mM potassium phosphate (pH 7.4) were investigated. In comparison with the reported stability of **DNIC-1** under an anaerobic condition,[45] a steady decay of the UV−vis absorption band at 362 nm under an aerobic condition reflects on the half-life of 15.5 ± 0.6 and 8.1 ± 0.7 h for **DNIC-1** under pH 7.4 and 6.8, respectively, at 37 °C (Figure 1a−d). This steady decomposition of **DNIC-1**, moreover, is coupled with the release of 4 equiv of nitric oxide without the transient formation of peroxynitrite (Figure 1e). In addition, S and Fe K-edge X-ray absorption spectroscopy (XAS) was utilized to probe the speciation of Fe and bridging $[HOCH_2CH_2S]^-$ ligands during the aerobic degradation of **DNIC-1**. As shown in Figure S1a, the S K-edge pre-edge absorption peaks at (2471.7, 2472.9) and 2474.8 eV exhibited by **DNIC-1** are ascribed to the transition from the S_{1s} orbital of the bridging $[HOCH_2CH_2S]^-$ ligands to the Fe_{3d} and C−S σ^* orbitals, respectively, which are consistent with those of other reported dinuclear DNICs $[(NO)_2Fe(\mu\text{-}SR)_2Fe(NO)_2]$.[46] Similar to other $\{Fe(NO)_2\}^9$ DNICs containing S-based ligands,[47] **DNIC-1** displays an $Fe_{1s}\rightarrow Fe_{3d}$ pre-edge absorption peak at 7113.9 eV (Figure S1b). After an aerobic degradation of **DNIC-1** in SIF, the disappearance of $S_{1s}\rightarrow Fe_{3d}$ transition peaks, the shift of the $S_{1s}\rightarrow$C−S σ^* transition peak from 2474.8 to 2474.1 eV, and the formation of the $S_{1s}\rightarrow$S−S σ^* transition peak at 2472.6 eV indicate the conversion of Fe-bound $[HOCH_2CH_2S]^-$ ligands into released $(SCH_2CH_2OH)_2$

https://doi.org/10.1021/jacsau.1c00160
JACS Au 2021, 1, 998−1013

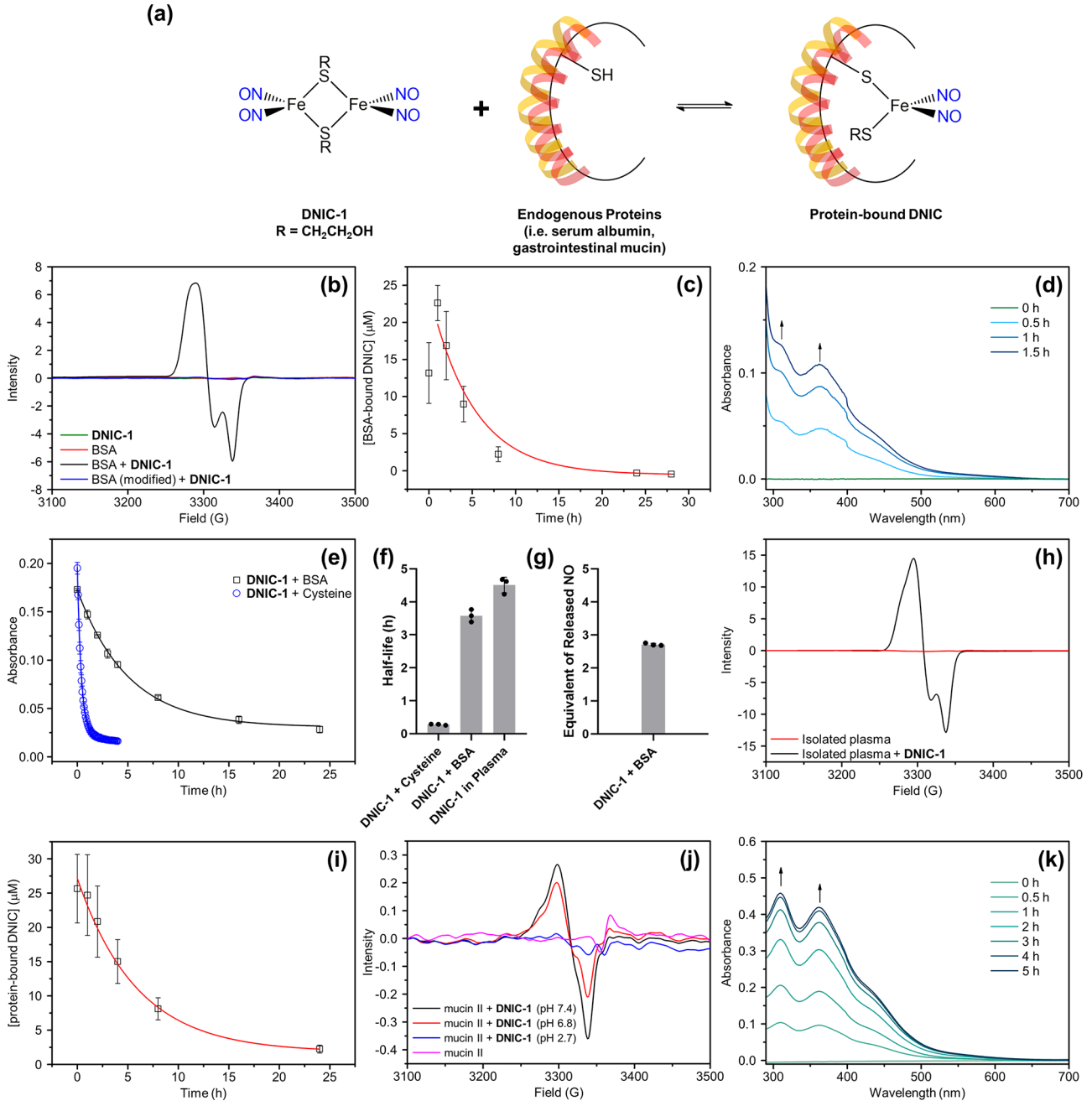

Figure 2. Reversible and dynamic interaction between **DNIC-1** and endogenous proteins. (a) Schematic illustration for reversible interaction between dinuclear **DNIC-1** and endogenous proteins leading to the assembly of protein-bound DNICs. (b) EPR spectra for **DNIC-1** in PBS (pH 7.4) with (black) or without (olive) the presence of BSA. EPR spectrum for reaction of **DNIC-1** with NEM-modified BSA in PBS (pH 7.4) is shown in blue, whereas the EPR spectrum of BSA is shown in red. (c) Formation and decay of BSA-bound DNIC derived from the reaction of **DNIC-1** and BSA in PBS (pH 7.4) at 37 °C, whereas the decay of BSA-bound DNIC was fitted to pseudo-first-order kinetics (red line). Data show the mean ± SD from three independent experiments. (d) Time-dependent change of UV−vis spectra for the PBS solution in the basolateral compartment of a dialysis tube, of which **DNIC-1** and BSA in PBS (pH 7.4) were added in the apical compartment. (e) Decompositions of **DNIC-1** with the presence of BSA (black) or L-cysteine (blue) in PBS (pH 7.4) under an aerobic condition at 37 °C, which were fitted to pseudo-first-order kinetics. Data show the mean ± SD from three independent experiments. (f) Half-life for **DNIC-1** with the presence of L-cysteine (or BSA) or in the isolated plasma at 37 °C. Data represent the mean ± SD ($n = 3$). (g) Equivalent of released NO after degradation of BSA-bound DNIC derived from the reaction of **DNIC-1** and BSA in PBS (pH 7.4). The data are the mean values ± the SD pooled from three independent experiments. (h) EPR spectra for isolated plasma with (black) or without (red) the presence of **DNIC-1**. (i) Decay of protein-bound DNIC derived from the addition of **DNIC-1** into the isolated plasma, which is fitted to pseudo-first-order kinetics (red line). Data represent the mean ± SD ($n = 3$). (j) EPR spectra for the reaction of **DNIC-1** and porcine stomach mucin in 100 mM phosphate buffer at pH 7.4 (black), pH 6.8 (red), and pH 2.7 (blue). EPR spectrum of porcine stomach mucin in 100 mM phosphate buffer at pH 7.4 is shown in magenta. (k) Time-dependent change of UV−vis spectra for the 100 mM phosphate buffer (pH 7.4) in the basolateral compartment of a dialysis tube, of which **DNIC-1** and porcine stomach mucin in 100 mM phosphate buffer (pH 7.4) were added in the apical compartment.

https://doi.org/10.1021/jacsau.1c00160
JACS Au 2021, 1, 998−1013

(Figure 1f). Moreover, the higher Fe K-edge pre-edge absorption energy at 7114.6 eV featured by the degradation byproducts supports the assembly of a ferric complex containing ionic ligands (i.e., phosphate, hydroxide, or oxide) after an aerobic degradation of **DNIC-1** in SIF (Figure 1g).[47,48] On the basis of the characterization of the released NO and S/Fe K-edge XAS study, a slow oxidation of the $[Fe(\mu\text{-}SR)_2Fe]$ core within **DNIC-1** under an aerobic condition initiates the transformation of bridging $[HOCH_2CH_2S]^-$ ligands into the released $(SCH_2CH_2OH)_2$, which weakens the Fe-to-NO π-backbonding interaction to trigger the complete release of nitric oxide and the assembly of a ferric complex (Scheme S1a).[37,46]

Upon incubation of **DNIC-1** in SGFsp at 37 °C, the shortened half-life of 0.4 ± 0.1 h and the reduced release of ∼2 equiv of nitric oxide reveal a distinctive mechanism for an accelerated decay of **DNIC-1** in SGFsp (Figure 1c−e,h). As shown in Figure 1i, an analysis of the gaseous byproduct derived from the degradation of **DNIC-1** in SGFsp by gas chromatography (GC) demonstrates the formation of $N_2O_{(g)}$, which is absent during the degradation of **DNIC-1** at pH 7.4 (or 6.8). During the degradation of **DNIC-1** in SGFsp, moreover, the S K-edge XAS transition peaks shift from 2471.7, 2472.9, and 2474.8 eV to (2472.8, 2474.0), 2475.1, 2477.8, and 2481.0 eV (Figure 1f). On the one hand, in comparison with the parent **DNIC-1** and other S-containing compounds, this shift of S K-edge XAS transition peaks indicates the dissociation and conversion of bridging $[HOCH_2CH_2S]^-$ ligands into $(SCH_2CH_2OH)_2$, $[HOCH_2CH_2SO]^-$, $[HOCH_2CH_2SONH_2]$, and $[HOCH_2CH_2SO_3]^-$ (Figure S1). On the other hand, the Fe K-edge pre-edge absorption energy at 7114.3 eV featured by the degradation byproducts, in contrast to that of 7113.9 eV exhibited by **DNIC-1**, also supports the dissociation of $[HOCH_2CH_2S]^-$ ligands and the assembly of an $[Fe^{III}-Cl]$ adduct, which displays a Cl K-edge pre-edge absorption peak at 2820.1 eV (Figure 1g,j). According to the study described above, the oxidation of **DNIC-1** in SGFsp results in the release of nitric oxide and the formation of $(SCH_2CH_2OH)_2$ as observed during the aerobic decomposition of **DNIC-1** at pH 6.8. In addition, the direct protonation of Fe-bound $[HOCH_2CH_2S]^-$ and NO ligands within **DNIC-1** under SGFsp initiates the generation of $HOCH_2CH_2SH$ and HNO, whereas the HNO further dimerizes to yield $N_2O_{(g)}$ or reacts with the generated thiol to afford $[HOCH_2CH_2SONH_2]$ (Scheme S1b).[49]

Reversible and Dynamic Interaction between DNIC-1 and Endogenous Proteins

Regarding the reported interconversion of DNICs between the low-molecular-weight and protein-bound forms, the reversible interaction of **DNIC-1** with endogenous proteins (i.e., bovine serum albumin (BSA) and porcine stomach mucin) and the stability of assembled protein-bound DNICs were further investigated (Figure 2a).[38,39,50] Upon titration of **DNIC-1** with bovine serum albumin in phosphate-buffer saline at pH 7.4 (PBS, pH 7.4), the decrease of the UV−vis absorption bands at (309, 362, 438) nm and the concomitant formation of UV−vis absorption bands at (384, 565) nm with two isosbestic points at (417, 493) nm unveiled the formation of a BSA-bound DNIC (Figure S2). EPR spectroscopy was further adopted to probe the nature of the dinitrosyl iron unit $[Fe(NO)_2]$ anchored in the BSA. As opposed to the EPR silence featured by both BSA and **DNIC-1**, the formation of a rhombic EPR signal at g = 2.044, 2.034, and 2.014 in the reaction of **DNIC-1** and BSA suggests the assembly of BSA-bound DNIC, which is comparable to that of biomimetic DNICs $[(NO)_2Fe(SR)(L)]^-$ and protein-bound DNICs derived from the reaction of $[(NO)_2Fe(Cys)_2]^-$ and BSA (Figure 2b and Table S1).[51] Moreover, this reaction of **DNIC-1** and BSA yielding BSA-bound DNIC reaches a plateau after a reaction for 15 min, whereas the subsequent decay of the indicative EPR signal under aerobic condition reflects a half-life of 3.5 ± 0.2 h (Figures 2c and S3). As shown in Figure 2b, the selective modification of the cysteine residue within the BSA by *N*-ethylmaleimide (NEM) inhibits the formation of this distinctive EPR signal. Considering the intrinsic binding affinity of a soft DNIU $[Fe(NO)_2]$ toward S-based ligands, consequently, the reaction of **DNIC-1** and BSA is proposed to lead to the assembly of mononuclear S = 1/2 $\{Fe(NO)_2\}^9$ DNIC $[(NO)_2Fe(SR)(BSA)]$ (R = CH_2CH_2OH) via the cleavage of dinuclear $\{Fe(NO)_2\}^9$-$\{Fe(NO)_2\}^9$ **DNIC-1** by the free thiol on Cys-34 within the BSA (Figure 2a).[24,52] Moreover, the spin quantitation of BSA-bound DNIC determines a 50% conversion of dinuclear **DNIC-1** into the protein-bound form using DNIC $[PPN][(NO)_2Fe(S_5)]$ as a standard (Figure S4). In the dialysis study of BSA-bound DNIC, a steady increase of the indicative UV−vis absorption bands at 309 and 362 nm for **DNIC-1** in the basolateral compartment of the dialysis system explored the reversible and dynamic interconversion between low-molecular-weight **DNIC-1** and BSA-bound DNIC (Figure 2d).[50] That is, the diffusion of the neutral and low-molecular-weight **DNIC-1** from the apical to basolateral compartment across the 3.5 kDa cutoff membrane of the dialysis system promotes the continued dissociation of an anchored $[(NO)_2Fe(SCH_2CH_2OH)]$ unit from the BSA, whereas the bridging nature of the $[HOCH_2CH_2S]^-$ thiolate ligand enables the reassembly of dinuclear **DNIC-1**. Assuming that the binding of **DNIC-1** toward BSA in a 1:2 stoichiometry leading to the assembly of 2 equiv of BSA-bound DNIC, the EPR study discussed above corresponds to an apparent equilibrium constant of 77.4 M^{-1}, while the stoichiometry for the reaction between **DNIC-1** and BSA awaits further crystallographic and spectroscopic investigations. Of interest, an apparent equilibrium constant of 285.7 M^{-1} for a similar dynamic equilibrium among $[(NO)_2Fe(\mu\text{-}S^tBu)_2Fe(NO)_2]$, $[S^tBu]^-$, and $[(NO)_2Fe(S^tBu)_2]^-$ in CH_3OH was also reported.[50]

In comparison with the anaerobic stability of BSA-bound DNIC in PBS (pH 7.4) at 37 °C, a steady decay of the UV−vis absorption bands at 384 and 565 nm under an aerobic condition reflects a half-life of 3.5 ± 0.3 h for the BSA-bound DNIC (Figures 2e,f and S5), which is consistent with that of 3.5 ± 0.2 h derived from the EPR experiments described above. Relevant to the aerobic degradation of **DNIC-1** described above, the oxidation of an Fe-bound $[HOCH_2CH_2S]^-$ thiolate ligand in the mononuclear S = 1/2 $\{Fe(NO)_2\}^9$ DNIC $[(NO)_2Fe(SR)(BSA)]$ (R = CH_2CH_2OH) may lead to the generation of the proposed DNIC $[(NO)_2Fe(BSA)]$ intermediate.[52,53] Presumably, the subsequent release of ∼1.4 equiv of nitric oxide from the DNIC $[(NO)_2Fe(BSA)]$ intermediate results in the ultimate formation of the $[Fe(BSA)]$ adduct (Figures 2g and S6).[52] The effect of free L-cysteine on the aerobic degradation of **DNIC-1** was also explored. On the basis of the concentration of free thiol on Cys-34 derived from 10 mg/mL of BSA, an addition of 150 μM L-cysteine to 25 μM **DNIC-1** shortens the half-life to 0.4 ± 0.1 h (Figures 2e,f and S7). As opposed to the stability of **DNIC-1** in the presence of BSA, this cysteine-accelerated decomposition of **DNIC-1** uncovered the stabilization effect of BSA on the delivery of DNIU $[Fe(NO)_2]$ and nitric oxide.

https://doi.org/10.1021/jacsau.1c00160
JACS Au 2021, 1, 998−1013

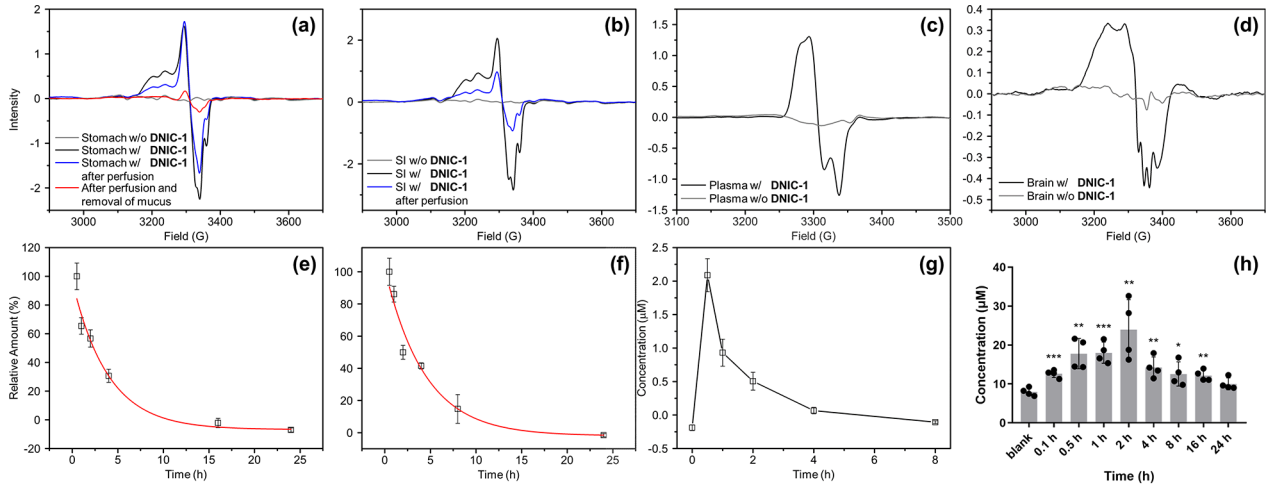

Figure 3. In vivo pharmacokinetic and biodistribution study of **DNIC-1** after an oral administration in mice. EPR spectra of (a) stomach (black), stomach after perfusion (blue), and stomach after perfusion and removal of mucus (red), (b) small intestine (black) and small intestine after perfusion (blue), (c) plasma (black), and (d) brain (black) isolated from the mice after an oral administration of **DNIC-1**. EPR spectra for each organ obtained from the mice without the treatment of **DNIC-1** are shown in gray. Time-dependent biodistribution study of **DNIC-1** in the (e) stomach and (f) small intestine characterized by EPR spectroscopy, whereas the fitting to pseudo-first-order kinetics is shown in red. The data are the mean values ± SEM (n = 3−5). (g) Pharmacokinetic study of **DNIC-1** in the plasma. The data are the mean values ± SEM (n = 3−5) (h) Time-dependent biodistribution study of nitric oxide in the brain. Data show the mean ± SEM from four independent experiments. *P < 0.05, **P < 0.01, and ***P < 0.001 compared to the concentration of nitric oxide in the brain of mice without the oral administration of **DNIC-1**. ID g^{-1} tissue, injected dose per gram of tissue.

With the addition of **DNIC-1** into the plasma isolated from mice, a similar EPR signal at g = 2.048, 2.033, and 2.014 supports the formation of a protein-bound DNIC (Figure 2h).[54] In comparison with BSA-bound DNIC featuring a rhombic EPR signal at g = 2.044, 2.034, and 2.014 (Table S1), this similar EPR feature suggested the serum albumin as the potential chaperone protein for the in vivo delivery of DNIU $[Fe(NO)_2]$ in the blood circulation system. As shown in Figure S8, 76−100% of **DNIC-1** was converted into the protein-bound form in the isolated plasma. Moreover, the fitting of the curve for the degradation of a protein-bound DNIC in the isolated plasma to a pseudo-first-order kinetic demonstrates a half-life of 4.5 ± 0.2 h (Figure 2f,i), which is comparable to that of 3.5 ± 0.2 h displayed by BSA-bound DNIC in PBS (pH 7.4).

As shown in Figures 2j and S9, the reaction of **DNIC-1** with porcine stomach mucin, a cysteine-rich protein in the gastrointestinal mucus,[14−17] at pH 7.4 or 6.8 promotes the rapid assembly of mucin-bound DNIC based on the generated EPR signal at g = 2.038, 2.028, and 2.014, which is relevant to biomimetic DNICs $[(NO)_2Fe(SR)(L)]^-$ (Table S1, L = thiolate, amido, imidazolate, carboxylate, or phenoxide). With the pretreatment of NEM to mucin, the reaction of **DNIC-1** and modified mucin results in the formation of a distinctive EPR signal at g = 2.052, 2.026, and 2.015 (Figure S10). That is, native porcine stomach mucin utilizes the cysteine residue(s) to promote the cleavage of dinuclear **DNIC-1** and to assemble the proposed mononuclear S = 1/2 $\{Fe(NO)_2\}^9$ DNIC $[(NO)_2Fe(SR)(mucin)]$ (R = CH_2CH_2OH). In comparison with biomimetic and peptide-/protein-bound DNICs (Table S1), different EPR features exhibited by BSA- and mucin-bound DNICs, presumably, can be ascribed to the alternative ligation modes, electron-donating ability of coordination ligands, binding angles of L-Fe-L, and local environment of the protein pockets for the tetrahedral $\{Fe(NO)_2\}^9$ center.

Similar to the reaction of **DNIC-1** and BSA, a reversible and dynamic interconversion between **DNIC-1** and mucin-bound DNICs was also evidenced by the dialysis study (Figure 2k). Moreover, a significant decrease of the distinctive EPR signal of a mucin-bound DNIC in the reaction of **DNIC-1** and mucin at pH 2.7 demonstrates the pH-dependent assembly of mucin-bound DNIC (Figure 2j), which is relevant to the formation of EPR-silent DNIC $[(NO)_2Fe(\mu\text{-}SPh)_2Fe(NO)_2]$ triggered by the protonation of the EPR-active DNIC $[(NO)_2Fe(SPh)_2]^-$.[55] A reliance on the intrinsic binding affinity of DNIU $[Fe(NO)_2]$ toward the cysteine residues in alternative proteins as well as the bridging capability of $[HOCH_2CH_2S]^-$ thiolate ligand in **DNIC-1**, consequently, a reversible and dynamic interconversion between the low-molecular-weight **DNIC-1** and protein-bound DNICs provides a mechanism for the stabilization and delivery of DNIU $[Fe(NO)_2]$.[50]

Oral Delivery of NO to Brain Enabled by Synergistic Interaction between DNIC-1 and Endogenous Protein Vehicles

Inspired by the reversible and dynamic interconversion between low-molecular-weight **DNIC-1** and protein-bound DNICs, the in vivo conjugation of **DNIC-1** with endogenous protein vehicles was explored using EPR spectroscopy. Meanwhile, pharmacokinetic and biodistribution profiles of protein-bound DNIC after an oral administration of **DNIC-1** to mice were also investigated to evaluate the efficacy for an oral delivery of NO to the brain. After an oral administration of **DNIC-1** to mice, a rhombic EPR signal at g = 2.041, 2.031, and 2.012 observed in the stomach demonstrates the instant formation of a protein-bound DNIC containing a mononuclear S = 1/2 $\{Fe(NO)_2\}^9$ unit (Figure 3a). In addition, the overlapped EPR signals at g = 2.07 and ∼2.01 (with $A \approx 17$ G), presumably, are ascribed to the accompanied formation of five-coordinate nitrosyl hemoglobin, which was also observed in the reported treatment of nitrite to gastric tissue.[56−58] After a perfusion of the stomach, the indicative EPR feature for the protein-bound DNIC remains active, while a significant decrease of this distinctive EPR feature was observed after a further removal of the mucus layer on the inner surface of stomach. Therefore, this distinctive EPR signal featured by gastrointestinal mucus discloses the rapid

https://doi.org/10.1021/jacsau.1c00160
JACS Au 2021, 1, 998−1013

association of **DNIC-1** to mucin and the assembly of mucin-bound DNIC embedded in the gastrointestinal mucus. On the other hand, the residual EPR signal at g = 2.040, 2.033, and 2.014 observed after the removal of the mucus layer may implicate the uptake of DNIU $[Fe(NO)_2]$ by the stomach tissue (Figure S11). As shown in Figure 3e, a time-dependent biodistribution study of **DNIC-1**, moreover, characterizes a half-life of 2.7 ± 0.6 h in the stomach, which shows a significant contrast to that of 0.4 ± 0.1 h for **DNIC-1** in SGFsp. Considering gastrointestinal mucus as a layer shielding the underlying epithelia from gastric fluid, as a consequence, the mucoadhesive nature of **DNIC-1**, derived from its rapid transformation into mucin-bound DNIC, provides a mechanism for the protection and temporal storage of DNIU $[Fe(NO)_2]$ in the gastrointestinal mucus layer of the stomach.[14−17]

On the basis of the time-dependent biodistribution study of **DNIC-1** in the small intestine, the formation and decay of the rhombic EPR signal at g = 2.040, 2.034, and 2.012 demonstrates a similar assembly of mucin-bound DNIC featuring a half-life of 3.0 ± 0.6 h (Figure 3b,f). In addition to the absence of protein-bound DNIC in the large intestine, the subsequent formation of an EPR signal at g = 2.048, 2.033, and 2.014 in the plasma suggests the systemic uptake and absorption of **DNIC-1** by the small intestine followed by an assembly of albumin-bound DNIC in the blood circulation system (Figures 3c and S12). It was reported that the interconversion among biomimetic DNICs $[(NO)_2Fe(SEt)_2]^-$, $[(NO)_2Fe(SPh)_2]^-$, and $[(NO)_2Fe(\mu\text{-}SPh)_2Fe(NO)_2]$ occurs through the thiolate ligand substitution and bridging-thiolate cleavage reactions.[36,37,50,55] After an oral administration of **DNIC-1**, presumably, a rapid binding of DNIU $[Fe(NO)_2]$ toward the mucin-derived cysteine within the gastrointestinal mucus layer of the stomach and small intestine rationalizes the enhanced gastrointestinal retention and improved stability of **DNIC-1** in the GI tract. Moreover, the reversible and dynamic nature of the bonding interaction between DNIU $[Fe(NO)_2]$ and cysteine ligands may offer a mucus-penetrating mechanism for the subsequent uptake and absorption of **DNIC-1** into the blood circulation system.

As discussed above, the oral administration and systemic absorption of **DNIC-1** inspired our utilization of human intestinal epithelial cell monolayer (Caco-2) as an in vitro model to dissect the mechanism for the permeability of **DNIC-1** across the epithelial barrier. As shown in Figure S13, **DNIC-1** features a half-maximal inhibitory concentration (IC_{50}) value of 39.3 ± 8.2 μM toward Caco-2 cells based on the Cell Counting Kit-8 (CCK-8) assay. Accordingly, an addition of 20 μM **DNIC-1** to the Caco-2 cell monolayers was performed to evaluate the paracellular permeability based on the transepithelial electrical resistance (TEER) experiments.[59] In comparison with the control group without any treatment, **DNIC-1** induces a time-dependent reduction of the TEER value, which recovers to the original level after a treatment of 24 h (Figure S13). Presumably, nitric oxide released from **DNIC-1** (or protein-bound DNIC) triggers a transient opening of the cellular tight junction to enhance the paracellular permeability of both **DNIC-1** and the protein-bound DNIC.[60] Regarding the LogP value of 1.0 for neutral and low-molecular-weight **DNIC-1**, a direct trafficking of **DNIC-1** across the intestinal epithelium via a transcellular mechanism cannot be excluded.

As shown in Figure 3g and Table S2, a pharmacokinetic study of **DNIC-1** in the plasma reflects a half-life of 0.9 ± 0.2 h, which is comparable to the reported value of 1.2 h after an intravenous injection of **DNIC-1**.[41] Through the comparison with the area under curve derived from pharmacokinetics of **DNIC-1** after an intravenous injection, the pharmacokinetics of **DNIC-1** after an oral administration characterizes an oral bioavailability of 6.5%. As opposed to the half-life of 4.5 ± 0.2 h for **DNIC-1** in isolated plasma, this in vivo half-life of 0.9 ± 0.2 h for **DNIC-1** in the plasma after oral administration is ascribed to its uptake by organs such as the liver and kidney (Figure S14). In contrast to the EPR silence observed in the brain isolated from the mice without the treatment of **DNIC-1**, of importance, the formation of the EPR signal at $g \approx 2.03$ supports the successful delivery of DNIU $[Fe(NO)_2]$ into the brain by an oral administration of **DNIC-1** (Figure 3d). Presumably, the overlapped EPR signals at g = (2.07, ~2.01 (with $A \approx 17$ G)) and (2.07, 1.98) are ascribed to the accompanied formation of five- and six-coordinate nitrosyl hemoglobin, which were also reported in the blood isolated from a rat after an intravenous injection of nitrite.[56,61] The subsequent release of nitric oxide from the DNIU $[Fe(NO)_2]$, moreover, results in the sustained elevation of the NO level in the brain, whereas the concentration of NO recovers to its original level after an oral administration of **DNIC-1** for 24 h (Figure 3h). After the oral administration of **DNIC-1** and its absorption across the intestinal epithelium, the mechanism for the subsequent trafficking in the blood circulation system and uptake by the brain are proposed below. In the blood circulation system, a stoichiometric conversion of **DNIC-1** into albumin-bound DNIC discovers serum albumin as an endogenous protein vehicle for the stabilization and delivery of DNIU $[Fe(NO)_2]$. Considering the reversible and dynamic interconversion between **DNIC-1** and albumin-bound DNIC, a direct transfer of low-molecular-weight and neutral **DNIC-1** (LogP = 1.0) across the blood-brain barrier (BBB) may occur through a transcellular pathway. Relevant to the transient opening of the cellular tight junction of a Caco-2 cell monolayer by **DNIC-1** described above, the enhanced paracellular permeability of the BBB promoted by NO-delivery **DNIC-1**, presumably, holds the potential to enable the subsequent release of nitric oxide from **DNIC-1** in the brain.[62]

In Vitro Antineuroinflammation and Pro-Neurogenic Effect of DNIC-1

Inspired by the successful delivery of nitric oxide to the brain using **DNIC-1**, in vitro antineuroinflammation and pro-neurogenic effects of **DNIC-1** on microglial and neuroblast cells, namely, BV-2 and N2A cells, were further evaluated. As shown in Figure 4a,b, **DNIC-1** exhibits the IC_{50} values of 11.7 ± 3.6 and 9.8 ± 0.6 μM toward BV-2 and N2A cells, respectively. Upon treatment of lipopolysaccharides (LPS, 1 μg/mL), the activation of BV-2 cells into a pro-inflammation state was evidenced by the elevated generation and secretion of cytokine tumor necrosis factor alpha (TNF-α, Figure 4c). Of importance, the intracellular release of nitric oxide from **DNIC-1** promotes an antineuroinflammation effect in LPS-activated microglial cells according to the suppressed level of secreted TNF-α upon treatment of **DNIC-1** (Figure 4c,d). On the other hand, the dose-dependent proliferation of neuroblast cells triggered by 2.5 μM (or 5 μM) **DNIC-1** demonstrates its potential application to neurogenesis (Figure 4b). In comparison with other NO donors (i.e., 2-(*N*,*N*-diethylamino)-diazenolate 2-oxide (DEA NONOate) and sodium nitroprusside (SNP), Figure S15), the distinctive pro-neurogenic effect of **DNIC-1** may be attributed to its different kinetics for the release of nitric oxide.[43,63−65] On the basis of the antineuroinflammation and pro-neurogenic

https://doi.org/10.1021/jacsau.1c00160
JACS Au 2021, 1, 998−1013

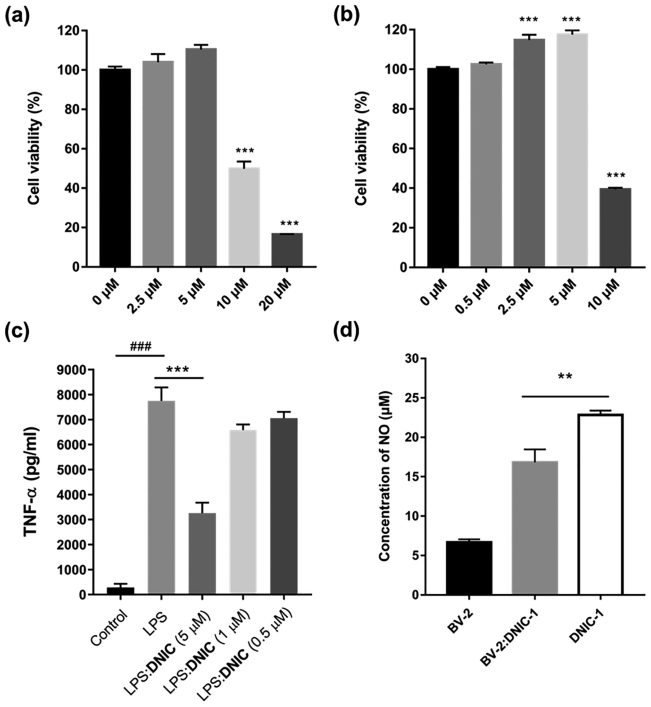

Figure 4. In vitro study of the antineuroinflammation and pro-neurogenesis effects of **DNIC-1**. Cell viability assay of the (a) BV-2 and (b) N2A cells treated with different concentrations of **DNIC-1** for 24 h. ***$P < 0.001$ compared to the group without treatment of **DNIC-1**. (c) Effect of **DNIC-1** on the production and secretion of TNF-α in LPS-activated BV-2. Data are presented as means ± SEM. $^{###}P < 0.001$ compared with the untreated control group. ***$P < 0.001$ compared with the group treated with LPS alone. (d) Concentration of nitric oxide in the supernatant culture media for BV-2 cells without (black) or with (gray) the treatment of 5 μM of **DNIC-1**. Concentration of nitric oxide in the medium with the treatment of **DNIC-1** (5 μM) is shown in white. **$P < 0.01$. In comparison with free **DNIC-1**, a significant decrease of nitric oxide in the supernatant culture media in the presence of BV-2 indicates the cellular uptake of **DNIC-1** and nitric oxide.

effects of **DNIC-1**, we are prompted to assess the therapeutic efficacy of **DNIC-1** on the recovery of cognitive ability in aging mice with metabolic syndrome.

DNIC-1 Activates Hippocampal Neurogenesis and Improves Cognitive Impairment in Aging Mice with Metabolic Syndrome

The utilization of aging mice under a Western diet (WD group) as a disease model for mild cognitive impairment and the protocol for the treatment are illustrated in Figure 5a.[66] According to the pharmacokinetics of nitric oxide in the brain after a treatment of **DNIC-1** and the pro-neurogenesis/antineuroinflammation effect, a daily treatment of **DNIC-1** at 2.65 mg/kg via an oral administration (WD:NO group) was performed in order to investigate the therapeutic efficacy of **DNIC-1**. As opposed to the aging mice under a control diet (CD group), a significant elevation of body weight and plasma glucose/serum triglyceride (TG)/serum cholesterol (TC) observed in the WD group indicates the successful induction of obesity and metabolic syndrome (Figure 5b–e and Table S3), which was reported to correlate with a cognitive impairment.[66] Through the comparison between WD and WD:NO groups, of interest, a decrease of serum glucose level induced by a daily treatment of **DNIC-1** is noticed.

After a treatment for 16 weeks, cognitive functions including spatial learning and memory of the aging mice in CD, WD, and WD:NO groups were further assessed using a Morris water maze task. The Morris water maze task is one of the most widely employed behavioral tests for the study of learning and memory in rodents. It depends on distal cues to crossing from start locations around the perimeter of an open swimming arena to locate a hidden escape platform.[66,67] During the acquisition phase of training (days 1–5 during week 17), all groups display a progressive decrease in latency to reach the hidden platform (Figure S16). When the hidden platform is removed during the probe trial, the duration for the aging mice staying in the target quadrant provides a quantitative evaluation on the ability of spatial learning and memory.[67] In comparison with the CD group, a significant decrease of duration in the target region displayed by aging mice in the WD group supports the cognitive impairment that resulted from Western diet-induced metabolic syndrome (Figure 5f). Of importance, a daily treatment of **DNIC-1** improves the cognitive impairment in aging mice with metabolic syndrome based on the increase of the duration in the target region featured by WD:NO group ($p = 0.217$ in comparison with WD group).

As shown in Figure 5g, a western blot analysis on the neuronal marker NeuN, proliferation marker BrdU, and microglial marker Iba1 in the hippocampus tissue was further performed in order to unravel the mechanism for the **DNIC-1**-induced improvement of the impaired cognitive ability. NeuN is a neuronal nucleus protein that begins to be expressed within the first few days of cell development and persists in mature neurons. BrdU is a thymidine analogue that can be incorporated into the proliferating cells during their DNA synthesis. After an injection of BrdU for one month, it has been reported that only newborn neurons remained immunoreactive.[68] Consequently, effect of **DNIC-1** on hippocampal neurogenesis was evaluated based on an immunoblot analysis of both NeuN and BrdU. In comparison with the aging mice under a control diet, the Western diet-induced obesity and metabolic syndrome imposes a neurotoxic effect and leads to the death of neural cells. Moreover, expression levels of NeuN and BrdU were significantly increased upon a daily treatment of **DNIC-1** (WD:NO group) when compared with WD group. That is, the pro-neurogenesis effect of the nitric oxide released from **DNIC-1** triggers the formation of newborn neurons in the hippocampus of aging mice in the WD:NO group. On the other hand, no significant difference between the levels of microglial marker Iba1 in the hippocampus tissues from CD, WD, and WD:NO groups were observed. In addition to the therapeutic effect of **DNIC-1** on the recovery of cognitive ability, serum chemistry analyses on the biomarkers for liver and kidney damage, that is, glutamic oxaloacetic transaminase (GOT), glutamic pyruvic transaminase (GPT), and creatinine (CRE), in CD, WD, and WD/NO groups demonstrate the biocompatibility of **DNIC-1** in aging mice under a metabolic syndrome (Figure 5h–k), although an elevation of uric acid (UA) in the WD:NO group is observed.

CONCLUSION

In this work, a mechanistic and efficacy study of the complex $[(NO)_2Fe(\mu\text{-}SCH_2CH_2OH)_2Fe(NO)_2]$ (**DNIC-1**) for an oral delivery of NO to brain, for activation of hippocampal neurogenesis, and for the recovery of cognitive ability of aging mice under a metabolic syndrome has led to the following results.

https://doi.org/10.1021/jacsau.1c00160
JACS Au 2021, 1, 998–1013

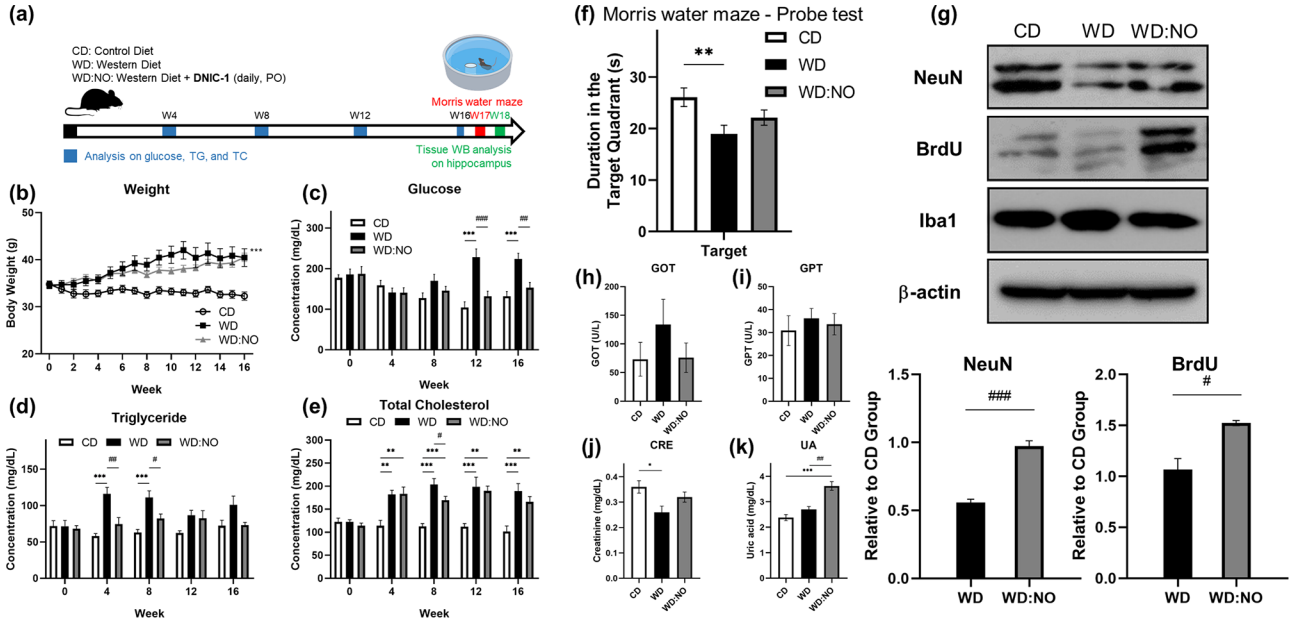

Figure 5. Activation of hippocampal neurogenesis and recovery of cognitive ability in aging mice with metabolic syndrome by **DNIC-1**. (a) Schematic illustration for the treatment protocol of **DNIC-1** to aging mice with metabolic syndrome. (b) Body weight, (c) serum glucose, (d) serum triglyceride (TG), and (e) serum total cholesterol (TC) observed in aging mice under control diet (CD), Western diet (WD), and WD in combination with daily treatment of **DNIC-1** (WD:NO). The data are the mean values ± SEM (n = 11−12 for body weight and n = 7−12 for glucose, TG, and TC in each group). (f) Duration for the aging mice staying in the target quadrant during the probe test in Morris water-maze task. Data show the mean ± SEM (n = 7−10 for each group). (g) Western blot analysis on the hippocampus tissue obtained from aging mice in CD, WD and WD:NO groups. The data are the mean values ± SEM (n = 3 for each group). NeuN is an indicator for neurons, BruU is an indicator for proliferation, Iba1 is an indicator for microglial cells, and β-actin is the internal control. (h) GOT, (i) GPT, (j) CRE, and (k) UA observed in aging mice under CD, WD, and WD:NO. Data show the mean ± SEM (n = 5 for each group). $^{*}P < 0.05$, $^{**}P < 0.01$, and $^{***}P < 0.001$ compared with the CD. $^{\#}P < 0.05$, $^{\#\#}P < 0.01$, and $^{\#\#\#}P < 0.001$ for comparison between WD and WD:NO.

1. The intrinsic binding affinity of DNIU $[Fe(NO)_2]$ toward the thiol group on the available cysteine residue of serum albumin promotes the in vitro and in vivo assembly of protein-bound DNIC $[(NO)_2Fe(SR)(BSA)]$ (R = CH_2CH_2OH) featuring a distinctive EPR signal at g = 2.03. Moreover, the bridging nature and capability of $[HOCH_2CH_2S]^-$ thiolate ligand enables the reversible and dynamic interconversion between the protein-bound DNIC and the low-molecular-weight **DNIC-1**. The oxidation of albumin-bound DNIC (or **DNIC-1**) results in the sustained release of NO without a transient formation of toxic peroxynitrite. As opposed to the accelerated decomposition of **DNIC-1** induced by free L-cysteine, serum albumin is discovered as an endogenous chaperone protein for the stabilization and delivery of DNIU $[Fe(NO)_2]$ in the blood circulation system.
2. Relevant to the in vitro binding of **DNIC-1** to porcine stomach mucin, the in vivo transformation of **DNIC-1** into mucin-bound DNIC within the gastrointestinal mucus layer after an oral administration explores the mucoadhesive nature of **DNIC-1** for the protection and temporal storage of DNIU $[Fe(NO)_2]$ in the stomach and small intestine. The reversible and dynamic nature of the bonding interaction between **DNIC-1** and mucus, moreover, offer a mucus-penetrating mechanism for the subsequent uptake and absorption of **DNIC-1** into the blood circulation system.
3. On the basis of the **DNIC-1**-induced reduction of the TEER value of a human intestinal epithelial cell monolayer, a transient opening of the cellular tight junction triggered by the nitric oxide released from **DNIC-1** enhances the paracellular permeability of **DNIC-1** (or protein-bound DNIC) across the intestinal epithelial barriers. On the other hand, a direct trafficking of neutral and low-molecular-weight **DNIC-1** (LogP = 1.0) across the intestinal epithelial and blood-brain barriers via a transcellular mechanism cannot be excluded. After an oral administration and a systematic absorption of **DNIC-1** across the intestinal epithelium, the subsequent trafficking of albumin-bound DNIC in the bloodstream and the transfer of DNIU $[Fe(NO)_2]$ into the brain complete the oral delivery of nitric oxide to the brain by **DNIC-1** and endogenous protein vehicles, namely, gastrointestinal mucin and serum albumin.
4. With aging mice under a Western diet as a disease model for metabolic syndrome and mild cognitive impairment, an oral administration of antineuroinflammatory and pro-neurogenic **DNIC-1** in a daily manner for 16 weeks activates hippocampal neurogenesis and ameliorates an impaired cognitive ability. On the other hand, serum chemistry analyses of GOT, GPT, and CRE support the biocompatibility of **DNIC-1**.

Instead of an exogenous conjugation/encapsulation of NO prodrugs with alternative drug delivery systems, in this study, the rapid and reversible binding of DNIU $[Fe(NO)_2]$ in low-molecular-weight **DNIC-1** toward the protein-derived cysteine discovers gastrointestinal mucin and serum albumin as endogenous protein vehicles for an oral delivery of nitric oxide to the brain. In addition to the discovery of **DNIC-1** as a therapeutic agent against a neurodegenerative condition, the interaction of alternative DNICs with endogenous protein vehicles and the development of exogenous DNIC/protein

https://doi.org/10.1021/jacsau.1c00160
JACS Au 2021, 1, 998−1013

conjugates for a controlled delivery of nitric oxide will be investigated in the near future.

MATERIALS AND METHODS

The reagents 3-mercaptopropionic acid ($HSCH_2CH_2COOH$) and iron chloride ($FeCl_3$) from Alfa Aesar; 3,3′-dithiodipropionic acid ($(SCH_2CH_2COOH)_2$), L-cysteine, *N*-ethylmaleimide (NEM), diethylamine NONOate sodium salt hydrate, heparin, porcine stomach mucin Type II (M2378), bovine serum albumin (BSA, A2153), anti-NeuN antibody (clone A60, MAB377), monoclonal anti-BrdU (clone BU33), anti-Iba1 antibody (SAB2702364), and β-actin from Sigma-Aldrich; the mouse TNF-α ELISA kit from RayBiotech; neuronal protein extraction reagent (N-PER) and Bradford assay kit from ThermoFisher Scientific; sodium chloride (NaCl) and cOmplete EDTA-free protease inhibitor sodium from Merck; 2-propene-1-sulfonic acid sodium salt ($CH_2CHCH_2SO_3Na$) from TCI; 2-methyl-2-propanesulfinamide ($(CH_3)_3CS(O)NH_2$) and sodium nitroprusside (SNP) from ACROS; sodium dihydrogen phosphate (NaH_2PO_4), disodium hydrogen phosphate (Na_2HPO_4), potassium dihydrogen phosphate (KH_2PO_4), and sodium hydroxide (NaOH) from Showa; hydrochloric acid (HCl, 37% w/v) from Fluka; and 2-amino-4-(methylsulfinyl)-butanoic acid ($CH_3S(O)CH_2CH_2CH(NH_2)COOH$) from Chemimpex, are of analytical grade and are used as received. Double-distilled water was obtained using a Millipore water distilling apparatus.

Simulated gastric and intestinal fluids were prepared and used in this study. Dissolution media that were used to simulate the gastric fluid are simulated gastric fluid without pepsin (SGFsp, USP 38; pH 1.2).[69] Dissolution media that were used to simulate the intestinal fluid are (a) simulated intestinal fluid without pancreatin (SIFsp, USP 26; pH 6.8) and (b) 0.05 M phosphate buffer (International Pharmacopeia, IntPh3; pH 7.4).[70]

Complexes $[(NO)_2Fe(\mu\text{-}SCH_2CH_2OH)_2Fe(NO)_2]$ (**DNIC-1**) and $[PPN][(NO)_2Fe(S_5)]$ (**DNIC-S$_5$**) were synthesized based on published procedures.[71] UV−Vis spectra were recorded on a PerkinElmer Lambda 365 spectrometer. The detection of gaseous byproduct(s) derived from the degradation of **DNIC-1** was performed on a Shimadzu GC-2030 gas chromatograph equipped with a barrier ionization discharge (BID) detector and Shinwa Micropacked-ST filled with Shincarbon-ST. $He_{(g)}$ was adopted as the carrier gas to conduct the sample separation. The oven was kept at 40 °C, and the detector was held at 280 °C.

Determination of LogP for DNIC-1

Double-distilled water (ddH_2O) and *n*-octanol were fully saturated with each other and degassed before use. After the addition of 200 μL of a 10 mM stock solution of **DNIC-1** in dimethyl sulfoxide (DMSO) to 19.8 mL of ddH_2O, 5 mL of this 100 μM **DNIC-1** solution was added with 3 mL of *n*-octanol. This mixture solution was vortexed thoroughly for 30 s and incubated until two solutions were separated. UV−Vis spectra of **DNIC-1** in ddH_2O before and after mixing with *n*-octanol were measured in order to determine the LogP using the equation shown below.[72]

$$\mathrm{LogP} = \log\left(\frac{A_0 - A_1}{A_1} \times \frac{V_w}{V_O}\right)$$

A_0 is the A_{362} in ddH_2O before partitioning, A_1 is the A_{362} in ddH_2O after partitioning, V_w = volume of ddH_2O used in partitioning, and V_o = volume of *n*-octanol used in partitioning.

Degradation and NO-Release Reactivity of DNIC-1 under Different pH Conditions

The aqueous solution for 25 μM **DNIC-1** was prepared via an addition of 20 μL of a 25 mM stock solution of **DNIC-1** in DMSO to 19.98 mL of 50 mM phosphate buffer, pH 7.4. After this solution was incubated at 37 °C under an aerobic condition for 0, 1, 2, 4, 8, 12, and 25 h, UV−vis spectra were measured in order to evaluate the degradation of **DNIC-1** based on the absorbance at 362 nm.[45] Assuming that the degradation of **DNIC-1** follows pseudo-first-order kinetics, the rate for the decrease of A_{362} was calculated to determine the half-life of **DNIC-1** in 50 mM phosphate buffer (pH 7.4) at 37 °C. Three independent experiments were executed to measure the average half-life for **DNIC-1**. The average half-life for **DNIC-1** in SIF and SGFsp, respectively, at 37 °C was determined in a similar manner.

After the incubation of 25 μM of **DNIC-1** in 50 mM phosphate buffer (pH 7.4), in SIF, and in SGFsp, respectively, under an aerobic condition for 2 d, the equivalent of nitric oxide released from the degradation of **DNIC-1** under alternative pH conditions was evaluated using Nitrate/Nitrite Colorimetric Assay Kit (Item No. 780001, Cayman). A general procedure is described below. After 10 μL of the aqueous solution derived from degradation of **DNIC-1** was diluted with 70 μL of kit assay buffer, 10 μL of Enzyme Cofactor Mixture (Item No. 780012) and 10 μL of Nitrate Reductase Mixture (Item No. 780010) were added before this mixture solution was covered and incubated at room temperature for 1 h. The subsequent addition of 50 μL of Griess Reagent R1 (Item No. 780018) and 50 μL of Griess Reagent R2 (Item No. 780020) followed by an incubation at room temperature for 15 min results in the formation of a UV−vis absorption band at 540 nm. The absorbance at 540 nm was then recorded using a microplate reader (SpectraMax iD3, Molecular Devices) with a reference wavelength of 800 nm. According to a calibration curve made with 0, 5, 10, 15, 20, 25, 30, and 35 μM nitrite standard (Item No. 780016)/nitrate standard (Item No. 780014), the equivalent of nitric oxide released from degradation of **DNIC-1** under alternative pH conditions was further estimated.

The generation of a gaseous byproduct (i.e., $N_2O_{(g)}$) during the degradation of **DNIC-1** in 50 mM phosphate buffer (pH 7.4), in SIF, and in SGFsp, respectively, was also characterized by gas chromatography (GC). After a 15 mL centrifuge tube loaded with 0.097 mg (0.25 μmol) of **DNIC-1** was sealed with a rubber septum, 10 mL of 50 mM phosphate buffer (pH 7.4) was added using a gastight syringe. This aqueous solution was further incubated for 2 d before 100 μL of the gas in the headspace of the sealed centrifuge tube was collected using a gastight syringe and analyzed by GC. Gaseous byproduct(s) derived from degradation of **DNIC-1** in SIF and SGFsp, respectively, were characterized in a similar manner.

The characterization of a transient formation of peroxynitrite during the degradation of **DNIC-1** in 50 mM phosphate buffer (pH 7.4) was attempted using 2,4-di-*tert*-butylphenol (DTBP) as a probe.[73] After the aqueous solution containing 25 μM **DNIC-1** and 100 μM DTBP was incubated at 37 °C under an aerobic condition for 2 d, the mixture solution derived from degraded **DNIC-1** was lyophilized before the crude product(s) was redissolved in 1 mL of dichloromethane (DCM). Analysis of this DCM solution by GC-MS indicated no formation of 2,4-di-*tert*-butyl-6-nitrophenol (NO_2-DTBP) from the nitration of DTBP, whereas the original substrate DTBP remained intact.

Characterization of Isolated and Degraded DNIC-1 by Fe, S, and Cl K-Edge X-ray Absorption Spectroscopy

After the degradation of **DNIC-1** in SIF and SGFsp, respectively, the aqueous solution containing degraded **DNIC-1** was lyophilized, whereas the obtained powder was further characterized by Fe, S, and Cl K-edge X-ray absorption spectroscopy (XAS). XAS experiments were performed at the National Synchrotron Radiation Research Center (NSRRC), Hsinchu, Taiwan. The isolated and degraded **DNIC-1** were ground to a powder and secured in a bag made of 6 μm Mylar film. The Fe K-edge XAS data were collected in fluorescence mode by using a seven-element silicon drift detector (SDD) at the TPS 44A beamline. The channel-cut Si(111) crystal is used to select the photon energy, and the standard Fe foil is used to calibrate the incident photon energy. The S and Cl K-edge XAS data were collected in fluorescence mode at BL 16A with a Si(111) monochromator. The energy resolution of the Si(111) diffraction plane $\Delta E/E$ is 1.4×10^{-4}. A Lytle detector was employed for fluorescence measurements in which the sample chamber is filled with high-purity He gas to avoid air absorption. The photon energy was calibrated to the maximum of the first pre-edge feature of $Na_2S_2O_3{\cdot}5H_2O$ at 2472.02 eV during the collection of S K-edge XAS, whereas the maximum of the first pre-edge feature of $CuCl_2$ at 2820.8 eV was adopted to calibrate the photon energy during the collection of Cl K-edge XAS. The energy is scanned

https://doi.org/10.1021/jacsau.1c00160
JACS Au 2021, 1, 998−1013

through 2.42−2.77 and 2.72−3.19 keV for the S and Cl K-edge XAS, respectively. Fe, S, and Cl K-edge XAS data were averaged, and a smooth background was removed from all spectra by fitting a straight line to the pre-edge region and subtracting this straight line from the entire spectrum. The normalization of the data was accomplished by fitting a flat polynomial to the postregion and normalizing the edge jump to 1.0.

Reaction of DNIC-1 with Bovine Serum Albumin or Porcine Stomach Mucin

Twenty-five micromolar **DNIC-1** in PBS (pH 7.4) was titrated with 0.25, 0.5, 0.75, 1.0, 1.25, 2.5, 5, 10, 25, and 50 mg/mL BSA and monitored by UV−vis spectroscopy after each titration. During the titration of **DNIC-1** with BSA, the decrease of the UV−vis absorption bands at 309, 362, and 438 nm and the concomitant formation of the UV−vis absorption band at 384 and 565 nm indicated the formation of BSA-bound DNIC. The formation of BSA-bound (or mucin-bound) DNIC derived from the reaction of **DNIC-1** (25 μM) with BSA (50 mg/mL) (or with mucin (1.6 mg/mL)) was also characterized by EPR. With DNIC [PPN][$(NO)_2Fe(S_5)$] as a standard, the formation of BSA-bound DNIC was quantified based on the calibration curve derived from the EPR spectra of 1, 2, 5, 10, 20, and 50 μM DNIC [PPN][$(NO)_2Fe(S_5)$] in tetrahydrofuran (THF).

The modification of BSA (or porcine stomach mucin) with *N*-ethylmaleimide was performed in the attempt to characterize the critical role of cystine residue(s) on the assembly of protein-bound DNICs. BSA in PBS (5 mg/mL, pH 7.4) was treated with 5 mg/mL NEM and incubated overnight at 4 °C. Afterward, 25 μM **DNIC-1** was further added into this PBS solution of NEM-modified BSA for EPR experiments. The modification of porcine stomach mucin (1.6 mg/mL) with NEM (10 mg/mL), reaction of NEM-modified mucin with **DNIC-1** (25 μM), and further EPR analysis were executed in a similar manner.

EPR Spectroscopy

In this study, all the EPR measurements were performed at the X-band using a Bruker EMXmicro-6/1/S/L spectrometer equipped with a Bruker E4119001 super high-sensitivity cavity. X-band EPR spectra were obtained with a microwave power of 20.27−20.54 mW, frequency at 9.41 GHz, conversion time of 66.68 ms, receiver gain of 30, and modulation amplitude of 10.0 G at 100 kHz.

Effect of BSA or L-Cysteine on the Degradation DNIC-1 in PBS (pH 7.4)

BSA-bound DNIC was prepared via an addition of 25 μM **DNIC-1** into 50 mg/mL BSA in PBS (pH 7.4). After this solution was incubated at 37 °C for 0, 1, 2, 4, 8, 24, and 28 h, respectively, EPR spectra of 100 μL aliquots of this solution were measured to quantify BSA-bound DNIC using DNIC [PPN][$(NO)_2Fe(S_5)$] as a standard. The time-dependent degradation of BSA-bound DNIC was then fit to pseudo-first-order kinetics in order to determine the half-life for BSA-bound DNIC in PBS (pH 7.4) at 37 °C. Three independent experiments were executed to measure the average half-life for BSA-bound DNIC under such condition.

The effect of BSA on the degradation **DNIC-1** in PBS (pH 7.4) was also evaluated using UV−vis spectroscopy. After an addition of 25 μM **DNIC-1** to 10 mg/mL BSA in PBS (pH 7.4), UV−vis spectra of this solution were measured after it was incubated at 37 °C under an aerobic condition for 0, 1, 2, 3, 4, 8, 16, and 24 h. Assuming that the degradation of **DNIC-1** follows pseudo-first-order kinetics, the rate for the decrease of A_{384} was calculated to determine the half-life of **DNIC-1** in the presence of 10 mg/mL BSA under pH 7.4 at 37 °C. Three independent experiments were executed to measure the average half-life for **DNIC-1** under such a condition. The average half-life for **DNIC-1** in the presence of 150 μM L-cysteine under pH 7.4 at 37 °C was determined in a similar manner.

The release of nitric oxide, generation of gaseous byproduct (i.e., $N_2O_{(g)}$), and absent formation of peroxynitrite during the degradation of 25 μM **DNIC-1** in the presence of BSA in PBS (pH 7.4) were characterized using Nitrate/Nitrite Colorimetric Assay Kit (Item No. 780001, Cayman), gas chromatography (GC), and DTBP as a peroxynitrite probe, respectively, as described above. Three independent experiments were executed to measure the average equivalent of released nitric oxide from **DNIC-1** in the presence of BSA.

After the degradation of 25 μM **DNIC-1** in the presence of 10 mg/mL BSA in PBS (pH 7.4), the formation of the [Fe(BSA)] adduct was characterized following the procedure below. The PBS solution containing the degraded **DNIC-1** was added into a spin column (molecular weight cut off [MWCO] 3 kDa, Merck) and centrifuged at 29 000 rpm for 10 min in order to remove the BSA and its adduct(s). This solution was then acidified with 10% HNO_3 before a further determination of Fe concentration by an Optima 8000 ICP-OES. The Fe concentration in the PBS solution of degraded BSA-bound DNIC without the removal of BSA by a spin column was also determined in the same manner.

Under an anaerobic condition, the stability of **DNIC-1** in PBS (pH 7.4) with the presence of 10 mg/mL BSA at 37 °C, namely, the BSA-bound DNIC, was also evaluated using UV−vis spectroscopy similar to the procedure described above. No change of the UV−vis spectra for the PBS solution of BSA-bound DNIC was observed after this solution was incubated for 24 h.

In Vitro Dialysis Release Study of BSA-Bound DNIC (or Mucin-Bound DNIC) at pH 7.4

BSA-bound DNIC derived from the reaction of 1 mM **DNIC-1** and 50 mg/mL BSA was loaded into the dialysis tube (MWCO 3.5 kDa, Gene Bioapplication Ltd.) before this dialysis system was placed in a release volume of 15 mL of PBS (pH 7.4) at 37 °C. After this dialysis system was incubated for 0, 0.5, 1, and 1.5 h, respectively, UV−vis spectra for the 700-μL aliquot of the PBS solution in the acceptor compartment were measured in order to monitor the release of **DNIC-1** from BSA-bound DNIC in the donor compartment. The acceptor compartment was refilled with 700 μL of fresh PBS (pH 7.4) after each measurement. An in vitro dialysis release study of the mucin-bound DNIC was performed in a similar manner using 1.6 mg/mL porcine stomach mucin.

Animals

C57BL/6JNarl (seven weeks old, male) for pharmacokinetic and biodistribution experiments were purchased from National Laboratory Animal Center (Taipei, Taiwan) and BioLASCO Taiwan Co., Ltd., whereas C57BL/6JNarl (12−15 months old, male) for aging mice with a metabolic syndrome were obtained from National Laboratory Animal Center. The animals were housed under a 12 h light/12 h dark cycle at a controlled temperature (22 ± 2 °C) and humidity (40 ± 10%), and provided with food and water ad libitum according to the Institutional Animal Care and Use Committee of Chung Yuan Christian University (permission Nos. 104010 and 108039) and National Tsing Hua University (permission No. 109048).

Stability of DNIC-1 in the Plasma Isolated from Mice

Mice were anaesthetized with an intraperitoneal injection of 2.5% tribromoethanol (Avertin) in diethylpyrocarbonate (DEPC) water and sacrificed. After a V-shaped cut was made through the skin and abdominal wall ∼1 cm caudal to the last rib, 700−1000 μL of blood samples were taken from the heart of each mouse using a 25G needle before the addition of 10% (v/v) heparin (1000 U/mL, Sigma-Aldrich) in order to avoid coagulation. To 4 mL of this fresh isolated blood sample, 4 μL of a DMSO stock solution of **DNIC-1** (25 mM) was added before this solution was incubated at 37 °C for 0, 1, 2, 4, 8, 24, and 28 h, respectively. At each time point, a 400 μL aliquot of this solution was transferred to a 1.5 mL Eppendorf tube and centrifuged at 3000 rpm for 10 min before the EPR spectrum for 100 μL of the supernatant solution was measured. On the basis of the calibration curve derived from the addition of 0, 1, 2, 5, 10, 20, and 50 μM of **DNIC-1** in the blood, the time-dependent degradation of protein-bound DNIC was then fit to pseudo-first-order kinetics in order to determine the half-life for **DNIC-1** in the blood isolated from mice. Three independent experiments were executed to measure the average half-life for **DNIC-1** in the blood isolated from mice.

https://doi.org/10.1021/jacsau.1c00160
JACS Au 2021, 1, 998−1013

Pharmacokinetic and Time-Dependent Biodistribution Study of DNIC-1 and Nitric Oxide

After the C57BL/6JNarl male mice were fed with **DNIC-1** (13.25 mg/kg) by oral gavage for 0.1, 0.5, 1, 2, 4, and 8 h, 200 μL of blood was collected from the facial vein and mixed with 50 μL of heparin (1000 U/mL, Sigma-Aldrich). This isolated blood was centrifuged at 3000 rpm for 10 min under 4 °C before the EPR spectrum for 100 μL of the supernatant solution was measured. On the basis of the calibration curve of **DNIC-1** in the blood described above, a pharmacokinetic curve of **DNIC-1** in mice was established from three independent experiments. The time-dependent decay of the EPR signal intensity after an oral administration of **DNIC-1** for 0.5 h was then fit to pseudo-first-order kinetics in order to determine the in vivo half-life for **DNIC-1** in the blood.

A time-dependent biodistribution study of **DNIC-1** was evaluated in a similar manner. After the C57BL/6JNarl male mice were fed with **DNIC-1** (13.25 mg/kg) by oral gavage for 0.1, 0.5, 1, 2, 4, 8, 16, and 24 h, the mice were sacrificed following the procedure described above. The stomach, small intestine, large intestine, liver, kidney, and brain, respectively, were collected and homogenized in a lysis buffer (10 mM Tris-HCl, 1% Triton X-100, 0.1% sodium dodecyl sulfate (SDS), 0.1% sodium deoxycholate, and 140 mM NaCl). The tissue lysates were kept on ice for 30 min and centrifuged at 25 000g at 4 °C for 30 min before the EPR spectrum for 100 μL of the supernatant solution was measured. The concentration of **DNIC-1** in each organ was further determined based on the calibration curve derived from an addition of different concentrations of **DNIC-1** into the corresponding organs.

With the brain lysates obtained as described above, the concentration of nitric oxide was further determined by a Nitrate/Nitrite Colorimetric Assay Kit (Item No. 780001, Cayman) in order to evaluate the time-dependent biodistribution study of nitric oxide in the brain after a treatment of **DNIC-1**. A general procedure is described below. A 500 μL aliquot of brain lysate was added into a spin column (MWCO 3 kDa, Merck) and centrifuged at 29 000 rpm for 10 min in order to remove the proteins from the brain lysates. The concentration of nitric oxide in this protein-free brain lysate was further determined using a Nitrate/Nitrite Colorimetric Assay Kit (Item No. 780001, Cayman) following the procedure described above.

Cells

Caco-2 human intestinal epithelial cell was provided by L.-W. Hsu (Food Industry Research and Development Institute, Taiwan). The Caco-2 cells were cultured in Minimum Essential Medium Eagle Alpha Modification (MEM Alpha) (Gibco) supplemented with 10% fetal bovine serum (FBS, Gibco) and 1% penicillin/streptomycin (Invitrogen); the BV-2 microglia cells were cultured in high-glucose Dulbecco's modified Eagle's medium (DMEM, Gibco) supplemented with 10% fetal bovine serum (Gibco), 2 mM glutamine (Gibco), and 1% penicillin/streptomycin (Invitrogen); and the N2A neuroblast cells were cultured in Minimum Essential Media (MEM) (Gibco) supplemented with 5% fetal bovine serum (Gibco), sodium pyruvate (Gibco), and 1% penicillin/streptomycin (Invitrogen). The Caco-2, BV-2, and N2A cells were incubated in a T75 flask at 37 °C in 5% CO_2 humidified air, and the culture medium was refreshed every other day.

Cell Viability Study of BV-2 Microglia, N2A Neuroblast Cells, and Caco-2 Intestinal Epithelial Cells

A cell viability study of a BV-2 microglia cell with or without the treatment of **DNIC-1** was measured using a Cell Counting Kit-8 (Dojindo, FoliBio) according to the manufacturer's protocol. Briefly, BV-2 microglia cells were seeded into a 96-well plate at a density of 1×10^4 cells/well and incubated overnight. The next day, BV-2 microglia cells were treated with **DNIC-1** at different concentrations (0, 2.5, 5, 10, 20, and 50 μM) and incubated for 24 h. Culture media were then removed before the BV-2 microglia cells were washed with DPBS. After the addition of fresh medium containing CCK-8 solution to the BV-2 microglia cells and an incubation for 1 h, the absorbance at 450 nm was then measured on a microplate reader (SpectraMax iD3, Molecular Devices) with a reference wavelength of 650 nm. Three independent experiments were executed, and the result was represented as mean ± standard error of measure (SEM) % (n = 3) with the untreated cells (control) as 100% viability. A cell viability study of N2A neuroblast and Caco-2 intestinal epithelial cells with or without the treatment of **DNIC-1** (or 2-(*N*,*N*-diethylamino)-diazenolate 2-oxide (DEA NONOate) and sodium nitroprusside (SNP)) for 24 h, respectively, was performed in a similar manner.

After the BV-2 microglia cells was treated with 5 μM **DNIC-1** for 2 h, the supernatant culture media were added into a spin column and centrifuged at 6000 rpm for 1 h. On the one hand, the concentration of nitric oxide in this protein-free supernatant culture media was further determined by a Nitrate/Nitrite Colorimetric Assay Kit (Cayman Chemical) following the procedure described below. On the other hand, the concentration of nitric oxide in the supernatant culture media derived from the BV-2 microglia cells without the treatment of **DNIC-1** was determined under a similar manner. Three independent experiments were executed, and the result was represented as the mean ± SEM relative to the untreated cells.

Transepithelial Electrical Resistance Measurements

The effect of **DNIC-1** on opening cellular tight junctions was investigated using Caco-2 cell monolayers cultured in transwell inserts (polycarbonate membrane, diameter of 6.5 mm and pore size of 0.4 μm, Costar-Corning Inc.) within 24-well plates. Transepithelial electrical resistance (TEER) values were measured using Millicell ERS-2 (Millipore) according to the manufacturer's instructions. Caco-2 cells were seeded on the membrane inserts at a density of 7.5×10^4 cells/cm^2. The apical and basolateral chambers were loaded with 0.2 and 0.6 mL of culture media, respectively, which was replaced every 2 d in the first week and every day in the following weeks. The formation of a cell monolayer was further evaluated by measuring the TEER values, whereas the results were calculated and corrected with blanks (DMEM with 10% FBS) using the equation shown below.

$$\mathrm{TEER}(\Omega \times \mathrm{cm}^2) = [\mathrm{TEER}_{\mathrm{sample}}(\Omega) - \mathrm{TEER}_{\mathrm{blank}}(\Omega)] \times \mathrm{area\ of\ membrane}(\mathrm{cm}^2)$$

After the Caco-2 cells were cultured for 21 d, the TEER values reached a plateau at 600−700 $\Omega \times$ cm^2 indicating the integrity of the cell monolayer. Caco-2 cells were then treated with 20 μM **DNIC-1** and incubated for 10, 30, and 60 min, respectively. The culture media in the upper and bottom chambers were replaced with fresh DMEM containing 10% FBS before measuring the TEER values.

In Vitro Anti-Inflammation Effect of DNIC-1 in LPS-Activated BV-2 Microglia Cells

The protein levels of TNF-α in culture medium were quantified by Mouse TNF-α ELISA kit (RayBiotech) following the manufacturer's protocol. Briefly, BV-2 microglia cells were seeded into a 24-well plate at a density of 1×10^5 cells/well and incubated overnight. The next day, BV-2 microglia cells were cotreated with LPS (1 μg/mL) and **DNIC-1** at different concentrations (0, 0.5, 1, and 5 μM) and incubated for 6 h. The supernatants were then transferred to the microplate wells coated with specific antibodies in advance (Mouse TNF-α ELISA kits, RayBiotech). Following the manufacturer's protocol, a sequential addition of biotinylated antibody, streptavidin solution, TMB One-Step Substrate Reagent, and stop solution was performed before the absorbance at 450 nm was measured on a microplate reader (SpectraMax iD3, Molecular Devices). The concentration of TNF-α (pg/mL) was further calculated based on the established calibration curve made with TNF-α standard.

Aging Mice with Metabolic Syndrome and Treatments

C57BL/6JNarl (12−15 months old, male) were purchased from National Laboratory Animal Center. The animals were housed under a 12 h light/12 h dark cycle at a controlled temperature (22 ± 2 °C) and humidity (40 ± 10%) and provided with food and water ad libitum according to the Institutional Animal Care and Use Committee of Chung Yuan Christian University. The mice were randomly divided into three groups, and each group received one of the following treatments for 16 weeks: (1) CD group, the control diet group was fed with LabDiet 5001 (containing 13.5% of kilocalories from fat and 3.7%

https://doi.org/10.1021/jacsau.1c00160
JACS Au 2021, 1, 998−1013

of kilocalories from sucrose) freely; (2) WD group, the Western diet group was fed with Diet Induced Obesity Rodent Purified Diet w/45% kilocalories from fat and 17% kilocalories from sucrose freely; (3) WD:NO group, the WD/NO group was fed with the same diet as that of the WD group and an additional treatment of **DNIC-1** (2.65 mg/kg) via an oral administration in a daily manner.

Serum Chemistry Analysis

Blood samples were collected every four weeks to measure the serum glucose, triacylglycerol (TG), total cholesterol, glutamate oxaloacetate transaminase (GOT), glutamic pyruvic transaminase (GPT), creatinine (CRE), and uric acid (UA). After coagulation, the mouse sera were collected from blood samples by a centrifugation at 10 000*g* for 20 min at 4 °C, and these sera samples were analyzed using a Fuji Dri-Chem 4000i analyzer at the Taiwan Mouse Clinic.

Morris Water Maze Test

The Morris Water Maze test was performed after a treatment for 16 weeks. The apparatus consisted of (1) a circular pool (diameter: 120 cm, height: 45 cm) filled with water (depth: 30 cm, 25 ± 0.5 °C) and (2) an escape platform (diameter: 10 cm) placed in the middle of one of the quadrants, 1 cm below the water surface and equidistant from the sidewall and the middle of the pool. The water tank was inside a test room containing spatial signs around the maze and remained undisturbed during the test. Each mouse was subjected to a series of four trials per day. For each trial, the mouse was placed into the water maze at four different positions. The trial began by placing the animal in the water facing the wall of the pool as one of the starting points. If the mouse failed to escape within 60 s, then it was gently directed to the platform. The mouse was allowed to stay on the platform for 15 s. The time between entering the water and climbing onto the platform was recorded as the latency to escape, and the average latency to escape was calculated for each mouse. The animals were trained for 5 d before the probe trial. The probe trial was performed on the sixth day by removing the platform from the pool. The mice were allowed to swim for 60 s, and the time spent in the target quadrant was recorded. After each trial, the mice were dried, and they were returned to their cages at the end of the session. The performances were recorded and analyzed using video-tracking software (Ethovision XT 7; Noldus Information Technology).

BrdU Administration

To observe the survival of newborn neurons from the hippocampal neurogenesis, the aging mice in CD, WD, or WD:NO groups were intraperitoneal injected with BrdU in a daily manner for three consecutive days (0.1 mg of BrdU per gram of body weight for aging mice, per dose). The aging mice were sacrificed after an additional one month before the immunoblot analysis on BrdU, NeuN, and Iba1 as described below.

Immunoblot Analysis

After the mice from CD, WD, and WD:NO groups were sacrificed, the isolated brain tissues were added with a neuronal protein extraction reagent (N-PER from ThermoFisher Scientific, with a ratio of 2000 μL/g tissue) and ethylenediaminetetraacetic acid (EDTA)-free protease inhibitor (from Sigma-Aldrich, with a ratio of 10 mL N-PER/ingot) before the tissues were homogenized with a tissue grinder. After complete homogenization, the tissue lysates were placed at 4 °C for 10 min and centrifuged at 10 000 rpm for 30 min. With BSA as a standard, a Bradford assay (from ThermoFisher Scientific) was further performed to determine the protein concentration in the tissue lysates. For further western blotting, the total protein (100 μg) isolated from the brain tissues was electrophoresed in a polyacrylamide/sodium dodecyl sulfate gel and transferred to a poly(vinylidene difluoride) (PVDF) membrane. The membrane was blocked with 5% nonfat milk in PBS for 1 h and then incubated overnight with primary antibodies against NeuN (Sigma-Aldrich, clone A60), BrdU (Sigma-Aldrich, clone BU33), Iba1 (Sigma-Aldrich, SAB2702364), or β-actin (Sigma-Aldrich) at 4 °C. After it was washed with PBST (0.1% Tween 20 in PBS), it was further incubated with the horseradish peroxidase (HRP)-conjugated secondary antibodies (Antibodies Inc.) for 1 h. The membrane was washed and developed by enhanced chemiluminescence using ECL plus (Thermo Scientific) followed by autoradiography.

Statistics

Statistical analyses (SD = standard deviation) were performed using GraphPad Prism 8. A one-way analysis of variance (ANOVA) followed by a Tukey post hoc test was used for the comparison of three or more groups. Values were normally distributed, and the variance was similar between compared groups. $P < 0.05$ was considered statistically significant. All behavioral data were processed and analyzed using Excel 2013 and SPSS software 20 (IBM Corp. IBM SPSS Statistics for Windows, ver. 20.0.). Several behavioral points exhibited a significant departure from normality, and the data for each of these points were rank-transformed, followed by a nonparametric Kruskal–Wallis test for intergroup comparisons.

■ ASSOCIATED CONTENT

Supporting Information

The Supporting Information is available free of charge at https://pubs.acs.org/doi/10.1021/jacsau.1c00160.

Scheme, figures, and tables for schematic illustration, additional experimental results including S/Fe K-edge XAS, UV–vis, EPR, ICP analysis, GC, cell viability assay, TEER, Morris water maze test, pharmacokinetic parameters, body weight and biochemical parameters of aging mice under different treatments, summary of EPR parameters for biomimetic, peptide-bound, and protein-bound $\{Fe(NO)_2\}^9$ DNICs (PDF)

■ AUTHOR INFORMATION

Corresponding Authors

Hung-Chi Chen − *Department of Ophthalmology and Center for Tissue Engineering, Chang Gung Memorial Hospital, Taoyuan, Taiwan; Department of Medicine, College of Medicine, Chang Gung University, Taoyuan, Taiwan*; Email: mr3756@cgmh.org.tw

Ting-Yu Chin − *Department of Bioscience Technology, Chung Yuan Christian University, Taoyuan, Taiwan*; Email: tychin@cycu.edu.tw

Tsai-Te Lu − *Institute of Biomedical Engineering, National Tsing Hua University, Hsinchu, Taiwan*; orcid.org/0000-0001-6977-2568; Email: ttlu@mx.nthu.edu.tw

Authors

Cheng-Ru Wu − *Institute of Biomedical Engineering, National Tsing Hua University, Hsinchu, Taiwan*

Yi-Da Huang − *Institute of Biomedical Engineering, National Tsing Hua University, Hsinchu, Taiwan; Department of Ophthalmology and Center for Tissue Engineering, Chang Gung Memorial Hospital, Taoyuan, Taiwan*

Yong-Huei Hong − *Institute of Biomedical Engineering, National Tsing Hua University, Hsinchu, Taiwan*

Ya-Hsin Liu − *Institute of Biomedical Engineering, National Tsing Hua University, Hsinchu, Taiwan*

Manmath Narwane − *Institute of Biomedical Engineering, National Tsing Hua University, Hsinchu, Taiwan*

Yu-Hsiang Chang − *Institute of Biomedical Engineering, National Tsing Hua University, Hsinchu, Taiwan*

Trinh Kieu Dinh − *Institute of Biomedical Engineering, National Tsing Hua University, Hsinchu, Taiwan*

Hsin-Tzu Hsieh − *Institute of Biomedical Engineering, National Tsing Hua University, Hsinchu, Taiwan*

Yi-Jen Hseuh − *Department of Ophthalmology and Center for Tissue Engineering, Chang Gung Memorial Hospital, Taoyuan, Taiwan*
Ping-Ching Wu − *Department of Biomedical Engineering, National Cheng Kung University, Tainan, Taiwan*
Chih-Wen Pao − *National Synchrotron Radiation Research Center, Hsinchu, Taiwan*
Ting-Shan Chan − *National Synchrotron Radiation Research Center, Hsinchu, Taiwan*
I-Jui Hsu − *Department of Molecular Science and Engineering, Research and Development Center of Smart Textile Technology, National Taipei University of Technology, Taipei, Taiwan;* orcid.org/0000-0001-5938-5783
Yunching Chen − *Institute of Biomedical Engineering, National Tsing Hua University, Hsinchu, Taiwan*

Complete contact information is available at: https://pubs.acs.org/10.1021/jacsau.1c00160

Author Contributions

○C.-R.W. and Y.-D.H. contributed equally.

Notes

The authors declare no competing financial interest.

■ ACKNOWLEDGMENTS

We gratefully acknowledge the financial support from the Ministry of Science and Technology, Taiwan (MOST 105-2815-C-033-007-B, MOST 108-2113-M-007-011, MOST 109-2628-M-007-003-MY3, MOST 109-2622-M-007-003-CC2, MOST 109-2320-B-033-001), from National Tsing Hua University, Taiwan (Grant Nos. 109Q2711E1, 110Q2711E1, and 110Q2513E1), and from Chang Gung Memorial Hospital (CMRPG3J0511, CMRPG3G0031-3). We thank National Synchrotron Radiation Research Center (Taiwan) for the support on Fe/S/Cl K-edge XAS experiments; K.-J. Hsing (Instrumentation Center, National Taiwan Normal University) for the help on EPR experiments; Y.-M. Li (National Chiao Tung University) for the help on GC-MS experiments; L.-W. Hsu (Food Industry Research and Development Institute, Taiwan) and C.-C. Huang (Institute of Biomedical Engineering, National Tsing Hua University) for the help on TEER experiments; the Taiwan Mouse Clinic (Academia Sinica and Taiwan Animal Consortium) for the technical support in serum chemistry analysis; and National Laboratory Animal Center, NARLabs, Taiwan, for technical support in animal experiments.

■ REFERENCES

(1) Lledo, P. M.; Alonso, M.; Grubb, M. S. Adult neurogenesis and functional plasticity in neuronal circuits. *Nat. Rev. Neurosci.* **2006**, *7* (3), 179−193.
(2) Contestabile, A.; Ciani, E. Role of nitric oxide in the regulation of neuronal proliferation, survival and differentiation. *Neurochem. Int.* **2004**, *45* (6), 903−914.
(3) Sharma, J. N.; Al-Omran, A.; Parvathy, S. S. Role of nitric oxide in inflammatory diseases. *Inflammopharmacology* **2007**, *15* (6), 252−259.
(4) Ha, K. S.; Kim, K. M.; Kwon, Y. G.; Bai, S. K.; Nam, W. D.; Yoo, Y. M.; Kim, P. K. M.; Chung, H. T.; Billiar, T. R.; Kim, Y. M. Nitric oxide prevents 6-hydroxydopamine-induced apoptosis in PC12 cells through cGMP-dependent PI3 kinase/Akt activation. *FASEB J.* **2003**, *17* (9), 1036−1047.
(5) Cooke, R. M.; Mistry, R.; Challiss, R. A. J.; Straub, V. A. Nitric Oxide Synthesis and cGMP Production Is Important for Neurite Growth and Synapse Remodeling after Axotomy. *J. Neurosci.* **2013**, *33* (13), 5626−5637.
(6) Choi, Y. K.; Maki, T.; Mandeville, E. T.; Koh, S. H.; Hayakawa, K.; Arai, K.; Kim, Y. M.; Whalen, M. J.; Xing, C.; Wang, X.; Kim, K. W.; Lo, E. H. Dual effects of carbon monoxide on pericytes and neurogenesis in traumatic brain injury. *Nat. Med.* **2016**, *22* (11), 1335−1341.
(7) Park, J.; Jin, K.; Sahasrabudhe, A.; Chiang, P. H.; Maalouf, J. H.; Koehler, F.; Rosenfeld, D.; Rao, S.; Tanaka, T.; Khudiyev, T.; Schiffer, Z. J.; Fink, Y.; Yizhar, O.; Manthiram, K.; Anikeeva, P. In situ electrochemical generation of nitric oxide for neuronal modulation. *Nat. Nanotechnol.* **2020**, *15* (8), 690−697.
(8) Jiang, Y. Q.; Fu, P. F.; Liu, Y. Y.; Wang, C. C.; Zhao, P. R.; Chu, X.; Jiang, X. W.; Yang, W.; Wu, Y. L.; Wang, Y.; Xu, G. H.; Hu, J.; Bu, W. B. Near-infrared light-triggered NO release for spinal cord injury repair. *Sci. Adv.* **2020**, *6* (39), eabc3513.
(9) Hua, Y.; Huang, X. Y.; Zhou, L.; Zhou, Q. G.; Hu, Y.; Luo, C. X.; Li, F.; Zhu, D. Y. DETA/NONOate, a nitric oxide donor, produces antidepressant effects by promoting hippocampal neurogenesis. *Psychopharmacology* **2008**, *200* (2), 231−242.
(10) Lu, D.; Mahmood, A.; Zhang, R.; Li, Y.; Chopp, M. Upregulation of neurogenesis and reduction in functional deficits following administration of DETA/NONOate, a nitric oxide donor, after traumatic brain injury in rats. *J. Neurosurg.* **2003**, *99* (2), 351−361.
(11) Coleman, C. I.; Limone, B.; Sobieraj, D. M.; Lee, S.; Roberts, M. S.; Kaur, R.; Alam, T. Dosing frequency and medication adherence in chronic disease. *J. Manag. Care. Pharm.* **2012**, *18* (7), 527−539.
(12) Kim, M. T.; Sedykh, A.; Chakravarti, S. K.; Saiakhov, R. D.; Zhu, H. Critical evaluation of human oral bioavailability for pharmaceutical drugs by using various cheminformatics approaches. *Pharm. Res.* **2014**, *31* (4), 1002−1014.
(13) Keseru, G. M.; Makara, G. M. The influence of lead discovery strategies on the properties of drug candidates. *Nat. Rev. Drug Discovery* **2009**, *8* (3), 203−212.
(14) Boegh, M.; Nielsen, H. M. Mucus as a Barrier to Drug Delivery − Understanding and Mimicking the Barrier Properties. *Basic Clin. Pharmacol. Toxicol.* **2015**, *116*, 179−186.
(15) Witten, J.; Samad, T.; Ribbeck, K. Selective permeability of mucus barriers. *Curr. Opin. Biotechnol.* **2018**, *52*, 124−133.
(16) Ensign, L. M.; Cone, R.; Hanes, J. Oral drug delivery with polymeric nanoparticles: the gastrointestinal mucus barriers. *Adv. Drug Delivery Rev.* **2012**, *64* (6), 557−570.
(17) Mitchell, M. J.; Billingsley, M. M.; Haley, R. M.; Wechsler, M. E.; Peppas, N. A.; Langer, R. Engineering precision nanoparticles for drug delivery. *Nat. Rev. Drug Discovery* **2021**, *20* (2), 101−124.
(18) Tian, H. K.; He, Z. Y.; Sun, C. X.; Yang, C. B.; Zhao, P. F.; Liu, L. X.; Leong, K. W.; Mao, H. Q.; Liu, Z. J.; Chen, Y. M. Uniform Core-Shell Nanoparticles with Thiolated Hyaluronic Acid Coating to Enhance Oral Delivery of Insulin. *Adv. Healthcare Mater.* **2018**, *7* (17), 1800285.
(19) Zhang, S. S.; Asghar, S.; Yu, F.; Chen, Z. P.; Hu, Z. Y.; Ping, Q. N.; Shao, F.; Xiao, Y. Y. BSA Nanoparticles Modified with N-Acetylcysteine for Improving the Stability and Mucoadhesion of Curcumin in the Gastrointestinal Tract. *J. Agric. Food Chem.* **2019**, *67* (33), 9371−9381.
(20) Han, X. F.; Lu, Y.; Xie, J. B.; Zhang, E. S.; Zhu, H.; Du, H.; Wang, K.; Song, B. Y.; Yang, C. B.; Shi, Y. J.; Cao, Z. Q. Zwitterionic micelles efficiently deliver oral insulin without opening tight junctions. *Nat. Nanotechnol.* **2020**, *15* (7), 605−614.
(21) Lamson, N. G.; Berger, A.; Fein, K. C.; Whitehead, K. A. Anionic nanoparticles enable the oral delivery of proteins by enhancing intestinal permeability. *Nat. Biomed. Eng.* **2020**, *4* (1), 84−96.
(22) Smith, D. A.; Di, L.; Kerns, E. H. The effect of plasma protein binding on in vivo efficacy: misconceptions in drug discovery. *Nat. Rev. Drug Discovery* **2010**, *9* (12), 929−939.
(23) Elsadek, B.; Kratz, F. Impact of albumin on drug delivery-new applications on the horizon. *J. Controlled Release* **2012**, *157* (1), 4−28.
(24) Liu, Z.; Chen, X. Simple bioconjugate chemistry serves great clinical advances: albumin as a versatile platform for diagnosis and precision therapy. *Chem. Soc. Rev.* **2016**, *45* (5), 1432−14356.
(25) Lin, T.; Zhao, P.; Jiang, Y.; Tang, Y.; Jin, H.; Pan, Z.; He, H.; Yang, V. C.; Huang, Y. Blood-Brain-Barrier-Penetrating Albumin Nanoparticles for Biomimetic Drug Delivery via Albumin-Binding

Protein Pathways for Antiglioma Therapy. *ACS Nano* **2016**, *10* (11), 9999−10012.
(26) Mayr, J.; Heffeter, P.; Groza, D.; Galvez, L.; Koellensperger, G.; Roller, A.; Alte, B.; Haider, M.; Berger, W.; Kowol, C. R.; Keppler, B. K. An albumin-based tumor-targeted oxaliplatin prodrug with distinctly improved anticancer activity in vivo. *Chem. Sci.* **2017**, *8* (3), 2241−2250.
(27) Tang, Y.; Yang, T.; Wang, Q.; Lv, X.; Song, X.; Ke, H.; Guo, Z.; Huang, X.; Hu, J.; Li, Z.; Yang, P.; Yang, X.; Chen, H. Albumin-coordinated assembly of clearable platinum nanodots for photo-induced cancer theranostics. *Biomaterials* **2018**, *154*, 248−260.
(28) Yang, J.; Wang, T.; Zhao, L.; Rajasekhar, V. K.; Joshi, S.; Andreou, C.; Pal, S.; Hsu, H. T.; Zhang, H.; Cohen, I. J.; Huang, R.; Hendrickson, R. C.; Miele, M. M.; Pei, W.; Brendel, M. B.; Healey, J. H.; Chiosis, G.; Kircher, M. F. Gold/alpha-lactalbumin nanoprobes for the imaging and treatment of breast cancer. *Nat. Biomed. Eng.* **2020**, *4* (7), 686−703.
(29) Zheng, Y.-R.; Suntharalingam, K.; Johnstone, T. C.; Yoo, H.; Lin, W.; Brooks, J. G.; Lippard, S. J. Pt(IV) prodrugs designed to bind non-covalently to human serum albumin for drug delivery. *J. Am. Chem. Soc.* **2014**, *136* (24), 8790−8798.
(30) Ma, J.; Wang, Q.; Huang, Z.; Yang, X.; Nie, Q.; Hao, W.; Wang, P. G.; Wang, X. Glycosylated Platinum(IV) Complexes as Substrates for Glucose Transporters (GLUTs) and Organic Cation Transporters (OCTs) Exhibited Cancer Targeting and Human Serum Albumin Binding Properties for Drug Delivery. *J. Med. Chem.* **2017**, *60* (13), 5736−5748.
(31) Pichler, V.; Mayr, J.; Heffeter, P.; Domotor, O.; Enyedy, E. A.; Hermann, G.; Groza, D.; Kollensperger, G.; Galanksi, M.; Berger, W.; Keppler, B. K.; Kowol, C. R. Maleimide-functionalised platinum(IV) complexes as a synthetic platform for targeted drug delivery. *Chem. Commun.* **2013**, *49* (22), 2249−2251.
(32) Warnecke, A.; Fichtner, I.; Garmann, D.; Jaehde, U.; Kratz, F. Synthesis and biological activity of water-soluble maleimide derivatives of the anticancer drug carboplatin designed as albumin-binding prodrugs. *Bioconjugate Chem.* **2004**, *15* (6), 1349−1359.
(33) Zeng, X.; Sun, J.; Li, S.; Shi, J.; Gao, H.; Sun Leong, W.; Wu, Y.; Li, M.; Liu, C.; Li, P.; Kong, J.; Wu, Y. Z.; Nie, G.; Fu, Y.; Zhang, G. Blood-triggered generation of platinum nanoparticle functions as an anti-cancer agent. *Nat. Commun.* **2020**, *11* (1), 567.
(34) Ekanger, L. A.; Oyala, P. H.; Moradian, A.; Sweredoski, M. J.; Barton, J. K. Nitric Oxide Modulates Endonuclease III Redox Activity by a 800 mV Negative Shift upon $[Fe_4S_4]$ Cluster Nitrosylation. *J. Am. Chem. Soc.* **2018**, *140* (37), 11800−11810.
(35) Bosworth, C. A.; Toledo, J. C., Jr.; Zmijewski, J. W.; Li, Q.; Lancaster, J. R., Jr. Dinitrosyliron complexes and the mechanism(s) of cellular protein nitrosothiol formation from nitric oxide. *Proc. Natl. Acad. Sci. U. S. A.* **2009**, *106* (12), 4671−4676.
(36) Hsiao, H.-Y.; Chung, C.-W.; Santos, J. H.; Villaflores, O. B.; Lu, T.-T. Fe in biosynthesis, translocation, and signal transduction of NO: toward bioinorganic engineering of dinitrosyl iron complexes into NO-delivery scaffolds for tissue engineering. *Dalton Trans.* **2019**, *48* (26), 9431−9453.
(37) Lu, T.-T.; Wang, Y.-M.; Hung, C.-H.; Chiou, S.-J.; Liaw, W.-F. Bioinorganic Chemistry of the Natural $[Fe(NO)_2]$ Motif: Evolution of a Functional Model for NO-Related Biomedical Application and Revolutionary Development of a Translational Model. *Inorg. Chem.* **2018**, *57* (20), 12425−12443.
(38) Cesareo, E.; Parker, L. J.; Pedersen, J. Z.; Nuccetelli, M.; Mazzetti, A. P.; Pastore, A.; Federici, G.; Caccuri, A. M.; Ricci, G.; Adams, J. J.; Parker, M. W.; Lo Bello, M. Nitrosylation of human glutathione transferase P1−1 with dinitrosyl diglutathionyl iron complex in vitro and in vivo. *J. Biol. Chem.* **2005**, *280* (51), 42172−42180.
(39) Rogers, P. A.; Ding, H. L-cysteine-mediated destabilization of dinitrosyl iron complexes in proteins. *J. Biol. Chem.* **2001**, *276* (33), 30980−30986.
(40) Pectol, D. C.; Khan, S.; Chupik, R. B.; Elsabahy, M.; Wooley, K. L.; Darensbourg, M. Y.; Lim, S. M. Toward the Optimization of Dinitrosyl Iron Complexes as Therapeutics for Smooth Muscle Cells. *Mol. Pharmaceutics* **2019**, *16* (7), 3178−3187.
(41) Sung, Y.-C.; Jin, P.-R.; Chu, L.-A.; Hsu, F.-F.; Wang, M.-R.; Chang, C.-C.; Chiou, S.-J.; Qiu, J. T.; Gao, D.-Y.; Lin, C.-C.; Chen, Y.-S.; Hsu, Y.-C.; Wang, J.; Wang, F.-N.; Yu, P.-L.; Chiang, A.-S.; Wu, A.-Y.; Ko, J.-J.; Lai, C.-P.; Lu, T.-T.; Chen, Y. Delivery of nitric oxide with a nanocarrier promotes tumour vessel normalization and potentiates anti-cancer therapies. *Nat. Nanotechnol.* **2019**, *14* (12), 1160−1169.
(42) Chazov, E. I.; Rodnenkov, O. V.; Zorin, A. V.; Lakomkin, V. L.; Gramovich, V. V.; Vyborov, O. N.; Dragnev, A. G.; Timoshin, C. A.; Buryachkovskaya, L. I.; Abramov, A. A.; Massenko, V. P.; Arzamastsev, E. V.; Kapelko, V. I.; Vanin, A. F. Hypotensive effect of Oxacom® containing a dinitrosyl iron complex with glutathione: animal studies and clinical trials on healthy volunteers. *Nitric Oxide* **2012**, *26* (3), 148−156.
(43) Chen, Y.-J.; Wu, S.-C.; Wang, H.-C.; Wu, T.-H.; Yuan, S.-F.; Lu, T.-T.; Liaw, W.-F.; Wang, Y.-M. Activation of Angiogenesis and Wound Healing in Diabetic Mice Using NO-Delivery Dinitrosyl Iron Complexes. *Mol. Pharmaceutics* **2019**, *16* (10), 4241−4251.
(44) Skodje, K. M.; Kwon, M.-Y.; Chung, S. W.; Kim, E. Coordination-triggered NO release from a dinitrosyl iron complex leads to anti-inflammatory activity. *Chem. Sci.* **2014**, *5*, 2374−2378.
(45) Huang, H.-W.; Lin, Y.-H.; Lin, M.-H.; Huang, Y.-R.; Chou, C.-H.; Hong, H.-C.; Wang, M.-R.; Tseng, Y.-T.; Liao, P.-C.; Chung, M.-C.; Ma, Y.-J.; Wu, S.-C.; Chuang, Y.-J.; Wang, H.-D.; Wang, Y.-M.; Huang, H.-D.; Lu, T.-T.; Liaw, W.-F. Extension of *C. elegans* lifespan using the center dot NO-delivery dinitrosyl iron complexes. *JBIC, J. Biol. Inorg. Chem.* **2018**, *23* (5), 775−784.
(46) Lu, T.-T.; Lai, S.-H.; Li, Y.-W.; Hsu, I.-J.; Jang, L.-Y.; Lee, J.-F.; Chen, I.-C.; Liaw, W.-F. Discrimination of mononuclear and dinuclear dinitrosyl iron complexes (DNICs) by S K-edge X-ray absorption spectroscopy: insight into the electronic structure and reactivity of DNICs. *Inorg. Chem.* **2011**, *50* (12), 5396−5406.
(47) Tsai, M.-C.; Tsai, F.-T.; Lu, T.-T.; Tsai, M.-L.; Wei, Y.-C.; Hsu, I.-J.; Lee, J.-F.; Liaw, W.-F. Relative Binding Affinity of Thiolate, Imidazolate, Phenoxide, and Nitrite Toward the $\{Fe(NO)_2\}$ Motif of Dinitrosyl Iron Complexes (DNICs): The Characteristic Pre-Edge Energy of $\{Fe(NO)_2\}^9$ DNICs. *Inorg. Chem.* **2009**, *48* (19), 9579−9591.
(48) Liu, P.-H.; Tsai, F.-T.; Chen, B.-H.; Hsu, I.-J.; Hsieh, H.-H.; Liaw, W.-F. Insight into chalcogenolate-bound $\{Fe(NO)_2\}^9$ dinitrosyl iron complexes (DNICs): covalent character versus ionic character. *Dalton Trans.* **2019**, *48*, 6040−6050.
(49) Bianco, C. L.; Toscano, J. P.; Bartberger, M. D.; Fukuto, J. M. The chemical biology of HNO signaling. *Arch. Biochem. Biophys.* **2017**, *617*, 129−136.
(50) Tsou, C.-C.; Lu, T.-T.; Liaw, W.-F. EPR, UV-Vis, IR, and X-ray demonstration of the anionic dimeric dinitrosyl iron complex $[(NO)_2Fe(\mu\text{-}S^tBu)_2Fe(NO)_2]^-$: relevance to the products of nitrosylation of cytosolic and mitochondrial aconitases, and high-potential iron proteins. *J. Am. Chem. Soc.* **2007**, *129* (42), 12626−12627.
(51) Boese, M.; Mordvintcev, P. I.; Vanin, A. F.; Busse, R.; Mulsch, A. S-nitrosation of serum albumin by dinitrosyl-iron complex. *J. Biol. Chem.* **1995**, *270* (49), 29244−29249.
(52) Pokidova, O. V.; Luzhkov, V. B.; Emel'yanova, N. S.; Krapivin, V. B.; Kotelnikov, A. I.; Sanina, N. A.; Aldoshin, S. M. Effect of albumin on the transformation of dinitrosyl iron complexes with thiourea ligands. *Dalton Trans.* **2020**, *49* (36), 12674−12685.
(53) Fitzpatrick, J.; Kalyvas, H.; Shearer, J.; Kim, E. Dioxygen mediated conversion of $\{Fe(NO)_2\}^9$ dinitrosyl iron complexes to Roussin's red esters. *Chem. Commun.* **2013**, *49* (49), 5550−5552.
(54) Timoshin, A. A.; Lakomkin, V. L.; Abramov, A. A.; Ruuge, E. K.; Kapel'ko, V. I.; Chazov, E. I.; Vanin, A. F. The hypotensive effect of the nitric monoxide donor Oxacom at different routs of its administration to experimental animals. *Eur. J. Pharmacol.* **2015**, *765*, 525−532.
(55) Lu, T.-T.; Chiou, S.-J.; Chen, C.-Y.; Liaw, W.-F. Mononitrosyl tris(thiolate) iron complex $[Fe(NO)(SPh)_3]^-$ and dinitrosyl iron complex $[(EtS)_2Fe(NO)_2]^-$: formation pathway of dinitrosyl iron

https://doi.org/10.1021/jacsau.1c00160
JACS Au 2021, 1, 998−1013

complexes (DNICs) from nitrosylation of biomimetic rubredoxin $[Fe(SR)_4]^{2-/1-}$ (R = Ph, Et). *Inorg. Chem.* **2006**, *45* (21), 8799−8806.
(56) Weinberg, J. B.; Gilkeson, G. S.; Mason, R. P.; Chamulitrat, W. Nitrosylation of blood hemoglobin and renal nonheme proteins in autoimmune MRL-*lpr/lpr* mice. *Free Radical Biol. Med.* **1998**, *24* (1), 191−196.
(57) Asanuma, K.; Iijima, K.; Ara, N.; Koike, T.; Yoshitake, J.; Ohara, S.; Shimosegawa, T.; Yoshimura, T. Fe-S cluster proteins are intracellular targets for nitric oxide generated luminally at the gastro-oesophageal junction. *Nitric Oxide* **2007**, *16* (4), 395−402.
(58) Ara, N.; Iijima, K.; Asanuma, K.; Yoshitake, J.; Ohara, S.; Shimosegawa, T.; Yoshimura, T. Disruption of gastric barrier function by luminal nitrosative stress: a potential chemical insult to the human gastro-oesophageal junction. *Gut* **2008**, *57*, 306−313.
(59) Lin, P.-Y.; Chuang, E.-Y.; Chiu, Y.-H.; Chen, H.-L.; Lin, K.-J.; Juang, J.-H.; Chiang, C.-H.; Mi, F.-L.; Sung, H.-W. Safety and efficacy of self-assembling bubble carriers stabilized with sodium dodecyl sulfate for oral delivery of therapeutic proteins. *J. Controlled Release* **2017**, *259*, 168−175.
(60) Salzman, A. L.; Menconi, M. J.; Unno, N.; Ezzell, R. M.; Casey, D. M.; Gonzalez, P. K.; Fink, M. P. Nitric oxide dilates tight junctions and depletes ATP in cultured Caco-2BBe intestinal epithelial monolayers. *Am. J. Physiol.* **1995**, *268*, G361−G373.
(61) Andreyev-Andriyevsky, A. A.; Mikoyan, V. D.; Serezhenkov, V. A.; Vanin, A. F. Penile erectile activity of dinitrosyl iron complexes with thiol-containing ligands. *Nitric Oxide* **2011**, *24* (4), 217−223.
(62) Weyerbrock, A.; Walbridge, S.; Saavedra, J. E.; Keefer, L. K.; Oldfield, E. H. Differential effects of nitric oxide on blood-brain barrier integrity and cerebral blood flow in intracerebral C6 gliomas. *Neuro. Oncol.* **2011**, *13* (2), 203−211.
(63) Li, B.; Ming, Y.; Liu, Y.; Xing, H.; Fu, R.; Li, Z.; Ni, R.; Li, L.; Duan, D.; Xu, J.; Li, C.; Xiang, M.; Song, H.; Chen, J. Recent Developments in Pharmacological Effect, Mechanism and Application Prospect of Diazeniumdiolates. *Front. Pharmacol.* **2020**, *11*, 923.
(64) Leeuwenkamp, O. R.; Chin, N. L. J.; van der Mark, E. J.; van Bennekom, W. P.; Bult, A. In vitro degradation of nitroprusside in relation to in vivo decomposition and mechanism of action. *Int. J. Pharm.* **1986**, *33*, 1−13.
(65) Majumder, S.; Sinha, S.; Siamwala, J. H.; Muley, A.; Reddy Seerapu, H.; Kolluru, G. K.; Veeriah, V.; Nagarajan, S.; Sridhara, S. R. C.; Priya, M. K.; Kuppusamy, M.; Srinivasan, S.; Konikkat, S.; Soundararajan, G.; Venkataraman, S.; Saran, U.; Chatterjee, S. A comparative study of NONOate based NO donors: Spermine NONOate is the best suited NO donor for angiogenesis. *Nitric Oxide* **2014**, *36*, 76−86.
(66) Tsai, Y.-C.; Lin, Y.-C.; Huang, C.-C.; Villaflores, O. B.; Wu, T.-Y.; Huang, S.-M.; Chin, T.-Y. Hericium erinaceus Mycelium and Its Isolated Compound, Erinacine A, Ameliorate High-Fat High-Sucrose Diet-Induced Metabolic Dysfunction and Spatial Learning Deficits in Aging Mice. *J. Med. Food* **2019**, *22* (5), 469−478.
(67) Tasi, Y.-C.; Chin, T.-Y.; Chen, Y.-J.; Huang, C.-C.; Lee, S.-L.; Wu, T.-Y. Potential Natural Products for Alzheimer's Disease: Targeted Search Using the Internal Ribosome Entry Site of Tau and Amyloid-beta Precursor Protein. *Int. J. Mol. Sci.* **2015**, *16* (4), 8789−8810.
(68) Palmer, T. D.; Willhoite, A. R.; Gage, F. H. Vascular niche for adult hippocampal neurogenesis. *J. Comp. Neurol.* **2000**, *425* (4), 479−494.
(69) Vertzoni, M.; Dressman, J.; Butler, J.; Hempenstall, J.; Reppas, C. Simulation of fasting gastric conditions and its importance for the in vivo dissolution of lipophilic compounds. *Eur. J. Pharm. Biopharm.* **2005**, *60* (3), 413−417.
(70) Arndt, M.; Chokshi, H.; Tang, K.; Parrott, N. J.; Reppas, C.; Dressman, J. B. Dissolution media simulating the proximal canine gastrointestinal tract in the fasted state. *Eur. J. Pharm. Biopharm.* **2013**, *84* (3), 633−641.
(71) Cho, S.-L.; Liao, C.-J.; Lu, T.-T. Synthetic methodology for preparation of dinitrosyl iron complexes. *JBIC, J. Biol. Inorg. Chem.* **2019**, *24* (4), 495−515.
(72) Medic-Saric, M.; Mornar, A.; Badovinac-Crnjevic, T.; Jasprica, I. Experimental and calculation procedures for molecular lipophilicity: A comparative study for 3,3′-(2-methoxybenzylidene)bis(4-hydroxycoumarin). *Croat. Chem. Acta* **2004**, *77* (1−2), 367−370.
(73) Lu, S.; Chiou, T.-W.; Li, W.-L.; Wang, C.-C.; Wang, Y.-M.; Lee, W.-Z.; Lu, T.-T.; Liaw, W.-F. Dinitrosyliron Complex $[(PMDTA)Fe(NO)_2]$: Intermediate for Nitric Oxide Monooxygenation Activity in Nonheme Iron Complex. *Inorg. Chem.* **2020**, *59*, 8308−8319.

https://doi.org/10.1021/jacsau.1c00160
JACS Au 2021, 1, 998−1013